

DYNAMICO-1.0, an icosahedral hydrostatic dynamical core designed for consistency and versatility

Thomas Dubos¹, Sarvesh Dubey², Marine Tort¹, Rashmi Mittal³,
Yann Meurdesoif⁴, and Frédéric Hourdin⁵

¹IPSL/Lab. de Météorologie Dynamique, École Polytechnique, Palaiseau, France

²Dept. of Mathematics, Indian Institute of Technology Delhi, Hauz Khas, New Delhi, India

³IBM India Research Laboratory, New Delhi, India

⁴IPSL/Lab. de Sciences du Climat et de l'Environnement, CEA-CNRS, Gif-sur-Yvette, France

⁵IPSL/Lab. de Météorologie Dynamique, CNRS - UPMC, Paris, France

Abstract. The design of the icosahedral dynamical core DYNAMICO is presented. DYNAMICO solves the multi-layer rotating shallow-water equations, a compressible variant of the same equivalent to a discretization of the hydrostatic primitive equations in a Lagrangian vertical coordinate, and the primitive equations in a hybrid mass-based vertical coordinate. The common Hamiltonian structure of these sets of equations is exploited to formulate energy-conserving spatial discretizations in a unified way.

The horizontal mesh is a quasi-uniform icosahedral C-grid obtained by subdivision of a regular icosahedron. Control volumes for mass, tracers and entropy/potential temperature are the hexagonal cells of the Voronoi mesh to avoid the fast numerical modes of the triangular C-grid. The horizontal discretization is that of Ringler et al. (2010), whose discrete quasi-Hamiltonian structure is identified. The prognostic variables are arranged vertically on a Lorenz grid with all thermodynamical variables collocated with mass. The vertical discretization is obtained from the three-dimensional Hamiltonian formulation. Tracers are transported using a second-order finite volume scheme with slope limiting for positivity. Explicit Runge-Kutta time integration is used for dynamics and forward-in-time integration with horizontal/vertical splitting is used for tracers. Most of the model code is common to the three sets of equations solved, making it easier to develop and validate each piece of the model separately.

Representative three-dimensional test cases are run and analyzed, showing correctness of the model. The design permits to consider several extensions in the near future, from higher-order transport to more general dynamics, especially deep-atmosphere and non-hydrostatic equations.

1 Introduction

In the last two decades a number of groups have explored the potential of quasi-uniform grids for overcoming well-known deficiencies of the latitude-longitude mesh applied to atmospheric general circulation modelling (Williamson, 2007). Particularly compelling has been the computational bottleneck created by the convergence of the meridians at the pole, which prevents efficient distribution of the computational load among many computers. Quasi-uniform grids have no such singular points and are free of this bottleneck. The first attempts at using quasi-uniform grids (Sadourny et al., 1968; Sadourny, 1972) failed at delivering important numerical properties that could be achieved on Cartesian longitude-latitude grids (Arakawa, 1966; Sadourny, 1975b, a; Arakawa and Lamb, 1981). For this reason the balance has been in favor of longitude-latitude grids until the recent advent of massively parallel computing provides a strong incentive to revisit these grids.

Since one reason for using quasi-uniform grids is the capability to benefit from the computing power of massively parallel supercomputers, many groups have set high-resolution modelling as a primary target. For the dynamical core, which solves the fluid dynamical equations of motion, this generally implies solving a non-hydrostatic set of equations. Indeed the hydrostatic primitive equations commonly used in climate-oriented GCMs assume that the modelled motions have horizontal scales much larger than the scale height, typically about 10km on Earth. Some hydrostatic models on quasi-uniform grids have been developed but essentially as a milestone towards a non-hydrostatic model (Wan et al., 2013).

In fact in many areas of climate research high-resolution modelling can still be hydrostatic. For instance paleo-climate modelling must sacrifice atmospheric resolution for simulation length, so that horizontal resolutions typical of CMIP-style climate modelling are so far beyond reach, and would definitely qualify as high-resolution for multi-millennial-scale simulations. Similarly, three-dimensional modelling of giant planets is so far unexplored since resolving their small Rossby radius requires resolutions of a fraction of a degree. Modelling at Institut Pierre Simon Laplace (IPSL) focuses to a large extent on climate time scales and has diverse interests ranging from paleoclimate to modern climate and planetology. When IPSL embarked in 2009 in an effort to develop a new dynamical core alongside LMD-Z (Hourdin et al., 2013), a medium-term goal was therefore set to focus on hydrostatic dynamics in order to best serve the IPSL community with increased efficiency and versatility.

By versatility it is meant the ability to relax in the dynamical core certain classical assumptions that are accurate for the Earth atmosphere but not necessarily for planetary atmospheres, or may have small but interesting effects on Earth. For instance in LMD-Z it is possible to assume for dry air a non-ideal perfect gas with temperature-dependent thermal capacities and this feature is used to model Venus (Lebonnois et al., 2010). In a similar vein a parallel effort has been undertaken to relax the shallow-atmosphere approximation in LMD-Z and solve the deep-atmosphere quasi-hydrostatic equations (White and Bromley, 1995; Tort and Dubos, 2014a). Although this feature is not yet im-

plemented in DYNAMICO, the same prognostic variables have been adopted in DYNAMICO as in the deep-atmosphere LMD-Z (Tort et al., 2014a), in order to facilitate upcoming generalizations of
60 DYNAMICO, including generalizations to non-hydrostatic dynamics.

LMD-Z is a finite-difference dynamical core but the kinematic equations (transport of mass, entropy/potential temperature, species) are discretized in flux-form, leading to the exact discrete conservation of total mass, total entropy/potential temperature and species content. Upwind-biased re-
65 constructions and slope limiters are used for the transport of species, which is consistent with mass transport and monotonic (Hourdin and Armengaud, 1999). Horizontal dynamics are discretized in vector-invariant form following the enstrophy-conserving scheme of Sadourny (1975a). Unlike the vast majority of hydrostatic dynamical cores, Simmons and Burridge (1981) is not used for vertical momentum transport and hydrostatic balance. Another discretization is used, which also preserves
70 exactly energy (Hourdin, 1994). Due to this emphasis on exact discrete conservation properties in LMD-Z a critical design goal of DYNAMICO was to have at least equivalent properties of conservation and consistency.

Pursuing both objectives of consistency and versatility (as defined above) implies that generic approaches must be found, rather than solutions tailored to a specific equation set. For instance the
75 equivalence of mass and pressure, the proportionality of potential and internal energies are valid only for the hydrostatic primitive equations and cease to be valid in a deep-atmosphere geometry, or even in a shallow-atmosphere geometry with a complete Coriolis force (Tort and Dubos, 2014a). The Bernoulli function appearing in the vector-invariant form of the equations of motion is the sum of kinetic energy and geopotential only if an ideal perfect gas (with temperature-independent thermal
80 capacities) is assumed (?). The same assumption is required to have internal energy and enthalpy proportional to temperature, as in Simmons and Burridge (1981). For versatility the dynamical core should not critically rely on such accidental relationships. This raises the question of what assumptions can be made that are both common to all potential target equation sets and sufficient to obtain the desired consistency properties. The answer to that question that has emerged during the DY-
85 NAMICO project is that the Hamiltonian formulation of the equations of motion is a sufficient common structure from which discrete consistency can be obtained for all well-formed equation sets. This idea is not really new. In fact it has been advocated for some time now by Salmon who applied it to the Saint-Venant equations (Salmon, 1983, 2004). However the Hamiltonian approach has been applied only once to date to derive a full-fledged three-dimensional dynamical core, by Gassmann
90 (2013). Gassmann (2013) uses the Hamiltonian formulation of the fully compressible equations in Eulerian coordinates. **This Hamiltonian theory has been recently extended for compressible hydrostatic flows and for non-Eulerian vertical coordinates (Tort and Dubos, 2014b; Dubos and Tort, 2014) and serves as the basis to formulate the discretization of dynamics in DYNAMICO.**

In addition to the above approach, building blocks for DYNAMICO include a positive definite
95 finite-volume transport scheme (Lauritzen et al., 2014a) and finite-difference operators generaliz-
ing Sadourny’s scheme to general unstructured spherical meshes. A partial generalization has been
achieved by Bonaventura and Ringler (2005) but still lacked a discrete conservation of potential
vorticity/potential enstrophy and exact discrete geostrophic equilibria, two properties tied together
as discussed by Thuburn (2008). A full generalization was obtained later by Thuburn et al. (2009);
100 Ringler et al. (2010) assuming a Delaunay-Voronoi pair of primal and dual meshes, or more gener-
ally orthogonal primal and dual meshes (see section 2). Thuburn et al. (2014) further generalize to
a wide class of non-orthogonal dual meshes, targeting the cubed sphere which has a better balance
between the degrees of freedom for mass and velocity, thus avoiding numerical modes present in tri-
angular meshes and their dual (Gassmann, 2011; Weller et al., 2012). However the accuracy of finite
105 differences on the cubed sphere is poor and a triangular-hexagonal grid yields much more accurate
results for a similar number of degrees of freedom than the cubed sphere (Thuburn et al., 2014). On
Delaunay-Voronoi meshes placing mass inside triangles leads to a branch of non-stationary numer-
ical modes which must be controlled by a non-trivial amount of dissipation (Rípodas et al., 2009;
Wan et al., 2013) while placing mass inside Voronoi domains leads to a stationary numerical modes
110 which requires no or very little dissipation for stable integrations (Ringler et al., 2010; Skamarock
et al., 2012; Gassmann, 2013). DYNAMICO follows the second option.

The present paper is organized as follows. Section 2 describes how the transport of mass, potential
temperature and other tracers is handled by DYNAMICO. For this the grid and the discrete repre-
sentation of scalar and vector fields are introduced. Mass fluxes through control volumes boundaries
115 are provided by the dynamics, as described in section 3. Following the Hamiltonian approach, the
primary quantity is the total energy, which is discretized first vertically then horizontally then yields
the discrete expressions for the Bernoulli function and other quantities appearing in the curl-form
equation of motion. Section 4 is devoted to energetic consistency. The discrete energy budget of
DYNAMICO is derived, and the underlying Hamiltonian structure of the TRiSK scheme (Thuburn
120 et al., 2009; Ringler et al., 2010) is identified. In section 5 sample numerical results are presented,
verifying the correctness of DYNAMICO and its ability to perform climate-style integrations. Our
main contributions are summarized and discussed in section 6, and future work is outlined.

2 Kinematics

In this section we describe how the transport of mass, potential temperature and other tracers is
125 handled by DYNAMICO, using mass fluxes computed by the dynamics as described in section 3.
We use bold face letters for vectors in three-dimensional physical space and for points on the unit
sphere. Space-dependent fields are functions of a vector \mathbf{n} on the unit sphere and a generalized
vertical coordinate η . Especially the geopotential $\Phi(\mathbf{n}, \eta, t)$ is a dependent quantity. Using the dot

notation for the Lagrangian (material) derivative, $\mathbf{u} = \dot{\mathbf{n}}$ is an angular velocity tangent to the unit sphere Σ , i.e. $\mathbf{n} \cdot \mathbf{u} = 0$. The Eulerian position \mathbf{r} of a fluid parcel in physical space is determined by the geopotential Φ considered as a vertical Eulerian coordinate and \mathbf{n} , i.e. $\mathbf{r} = \mathbf{r}(\Phi, \mathbf{n})$. An expression for $\mathbf{r}(\Phi, \mathbf{n})$ is not needed to solve the transport equations and needs to be specified only when dealing with the dynamics (see section 3). Denoting $\partial_\alpha = \partial/\partial\alpha$ for $\alpha = \mathbf{n}, \eta, t$, the continuous flux-form budget for mass, potential temperature θ and tracer q are

$$\partial_t \mu + \partial_{\mathbf{n}} \cdot \mathbf{U} + \partial_\eta W = 0, \quad (1)$$

$$\partial_t \Theta + \partial_{\mathbf{n}} \cdot (\theta \mathbf{U}) + \partial_\eta (\theta W) = 0. \quad (2)$$

$$\partial_t Q + \partial_{\mathbf{n}} \cdot (q \mathbf{U}) + \partial_\eta (q W) = 0. \quad (3)$$

where μ is the pseudo-density such that total mass is $\int \mu d^2 \mathbf{n} d\eta$, $\Theta = \mu\theta$, $Q = \mu q$, $\mathbf{U} = \mu \mathbf{u}$ is the horizontal **mass flux vector**, $W = \mu \dot{\eta}$ is the **mass flux per unit surface** through model layers $\eta = cst$.

The following subsections describe the grid, indexing conventions, the discrete mass and potential temperature budgets, and finally the positive-definite finite-volume scheme used for additional tracers.

2.1 Icosahedral-hexagonal grid, staggering and discrete objects

The mesh is based on a tessellation of the unit sphere (Sadourny et al., 1968). Each triangle has a global index v and each vertex has a global index i . Several points are associated to each index i or v . Mesh generation and smoothing is described in Appendix A and numerical stability issues arising in the calculation of spherical geometric entities are raised and solved in Appendix B. By joining v -points one obtains the hexagonal-pentagonal mesh, with control volumes indexed by i and vertices indexed by v . Mass will be associated with hexagonal control volumes and i -points, so we will refer to this mesh as the primal mesh, while the triangular mesh will be referred to as dual. Additional quantities are associated to primal edges joining v -points, and dual edges joining i -points. Both types of edges are indexed by e . These notations follow Thuburn et al. (2009). Lorenz staggering is used in the vertical. Full vertical levels are indexed by $k = 1 \dots K$. Interfaces between full levels are indexed by $l = 1/2 \dots L = K + 1/2$.

Following the spirit of **discrete exterior calculus** (DEC, see e.g. Thuburn and Cotter, 2012), we associate to each scalar or vector field a discrete description reflecting the underlying differential-geometric object, i.e. 0-forms (scalar functions), 1-forms (vector fields with a curl), 2-forms (vector fields with a divergence) and 3-forms (scalar densities). Scalar densities include μ and Θ . We describe them by discrete values μ_{ik}, Θ_{ik} defined as their integral over the three-dimensional control volumes (μ_{ik} is in units of kg). Scalar functions include $\theta_{ik} = \Theta_{ik}/\mu_{ik}$ and specific volume $\alpha_{ik} = \delta_k \Phi_i / (g \mu_{ik})$. 2-forms include the fluxes of mass and potential temperature. The horizontal mass flux vector $\mathbf{U} = \mu \mathbf{u}$ is described by its integrals U_{ek} over a vertical boundary between two

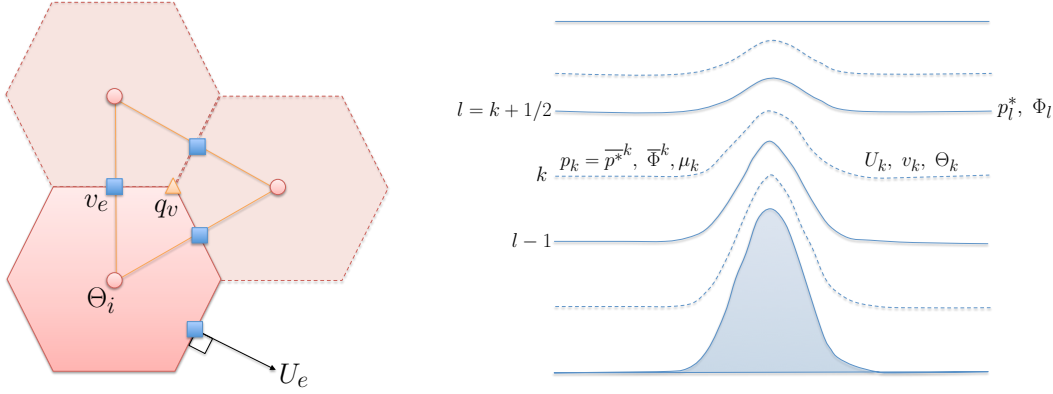


Figure 1: Staggering and location of key prognostic and diagnostic variables.

165 hexagonal control volumes and the vertical mass flux per unit surface $W = \mu\eta$ by its integral W_{il}
over the pseudo-horizonal boundary between two adjacent control volumes located one above an-
other (unit : kg/s).

Averages and finite differences are decorated with the location of the result, i.e. $\delta_k \Phi$ lies at full lev-
els, \bar{m}^l lies at interfaces, and $\bar{\Phi}^{ek}$ is collocated with U_{ek} (see Fig. 1). Especially, using the notations
170 of Ringler et al. (2010)

$$\delta_i U_k = - \sum_{e \in EC(i)} n_{ei} U_{ek}, \quad \delta_e \Phi_k = \sum_{i \in CE(e)} n_{ei} \Phi_{ik}, \quad \delta_v v_k = \sum_{e \in EV(v)} t_{ev} v_{ek}.$$

Operators δ_i , δ_e and δ_v are discrete versions of the two-dimensional div, grad and curl operators.
They are mimetic in the sense that they satisfy for any A_e , B_i the discrete formulae :

$$\sum_e A_e \delta_e B + \sum_i B_i \delta_i A = 0 \tag{4}$$

$$175 \quad \delta_v (\delta_e B) = 0 \tag{5}$$

(4) is a discrete integration-by-parts formula and (5) imitates $\text{curl grad} = 0$ (Bonaventura and Ringler,
2005). **Notice that the generic A, B used here are unrelated to quantities A (areas) and B (Bernoulli
function) defined later.**

2.2 Discrete mass, potential temperature and tracer budgets

180 The discrete mass and budget and potential temperature budgets are written in flux-form :

$$\partial_t \mu_{ik} + \delta_i U_k + \delta_k W_i = 0, \tag{6}$$

$$\partial_t \Theta_{ik} + \delta_i (\theta_k^* U_k) + \delta_k (\theta_i^* W_i) = 0, \tag{7}$$

where we omit certain indices when there is no ambiguity (e.g. in (6) we omit the index e of θ_{ek}^* and
 W_{ek} since operator δ_i is always applied to quantities located on edges) and θ_{ek}^* , θ_{il}^* are values of θ

185 reconstructed at interfaces between control volumes. Currently simple centered averages are used :

$$\theta_{il} = \frac{\Theta_{ik}}{\mu_{ik}}, \quad \theta_{ek}^* = \overline{\theta_k^e}, \quad \theta_{il}^* = \overline{\theta_i^l} \quad (8)$$

but it would be possible to use more accurate, possibly upwind biased, reconstructions as in finite volume advection schemes. **Indeed, as shown by Gassmann (2013), conserving discrete energy is possible when upwinding the advection of θ provided the same reconstructed values are reused in the curl-form momentum equation (see 4.2).**

190 Either a Lagrangian vertical coordinate or a mass-based vertical coordinate can be used. In the former case $W = 0$. Notice that if $W = 0$ and $\theta_{ik} = \theta_k$ is initially uniform, it will remain so at later times for adiabatic motion. This corresponds to using an isentropic/isopycnal vertical coordinate. In the latter case (mass-based vertical coordinate) only the column-integrated mass M_i is prognostic, while μ_{ik} is diagnosed from M_i :

$$M_i = \sum_k \mu_{ik}, \quad \mu_{ik} = -M_i \delta_k a - \delta_k b \quad (9)$$

with a_l, b_l predefined profiles satisfying $a = 0, b = 0$ at the top and $a = 1, b = 0$ at the bottom. Then summing (10) over k and using no-flux top and bottom boundary conditions for W provides a prognostic equation for M_i :

$$200 \quad \partial_t M_i + \delta_i \sum_k U_k = 0. \quad (10)$$

Once $\partial_t M_i$ hence $\partial_t \mu_{ik} = (\delta_k a) \partial_t M_i$ have been determined, (10) complemented by boundary conditions $W = 0$ at top and bottom is a diagnostic equation for W_{il} .

(6-7) are marched in time together with the dynamics using a Runge-Kutta time scheme with a time step τ (see section 3). On the other hand the additional tracers q are weakly coupled to the dynamics and can be stepped forward with a larger time step $\Delta t = N_{transport} \tau$ with $1/N_{transport}$ larger than the maximum Mach number in the flow. To this end, using simple bookkeeping, the dynamics provide time-integrated fluxes $\overline{U_{ek}}, \overline{W_{il}}$ (both in units of kg) such that :

$$\delta_t \mu_{ik} + \delta_i \overline{U_k} + \delta_k \overline{W_i} = 0 \quad (11)$$

210 where δ_t is a finite difference over $N_{transport}$ full Runge-Kutta time steps. Then (2) is discretized using horizontal-vertical splitting (Easter, 1993; Hourdin and Armengaud, 1999) :

$$\begin{aligned} Q_{ik}^{(1)} &= Q_{ik}^{(0)} - \frac{1}{2} \delta_k \left(q_i^{(0)} \overline{W_i} \right) \\ \mu_{ik}^{(1)} &= \mu_{ik}^{(0)} - \frac{1}{2} \delta_k \overline{W_i} \\ Q_{ik}^{(2)} &= Q_{ik}^{(1)} - \delta_i \left(q_e^{(1)} \overline{U_e} \right) \\ \mu_{ik}^{(2)} &= \mu_{ik}^{(1)} - \delta_i \overline{U_e} \\ 215 \quad Q_{ik}^{(3)} &= Q_{ik}^{(2)} - \frac{1}{2} \delta_k \left(q_i^{(2)} \overline{W_i} \right) \end{aligned}$$

where Q_{ik} is the cell-integrated value of $q\mu$ (in kg), $Q_{ik}^{(0)}$ (resp. $Q^{(3)}$) is the value of Q_{ik} at old time t (resp. new time $t + N_{transport}\tau$), $Q_{ik}^{(m)}, \mu_{ik}^{(m)}$ for $m = 1, 2$ are intermediate values, and $q^{(m)}$ are point-wise values of the tracer reconstructed from $Q^{(m)}$ and $\mu^{(m)}$ (see below). The reconstruction operators satisfy the consistency principle that $q^{(m)} = 1$ whenever $Q^{(m)} = \mu^{(m)}$. As a result $Q^{(3)} = \mu^{(3)}$ whenever $Q^{(0)} = \mu^{(0)}$, i.e. the tracer budget is consistent with the mass budget.

The vertical reconstruction is one-dimensional, piecewise-linear, slope-limited, and identical to Van Leer's scheme I (Van Leer, 1977; Hourdin and Armengaud, 1999). The horizontal advection scheme is identical to SLFV-SL of Lauritzen et al. (2012) and is detailed in (Dubey et al., 2015). It relies on cell-wise linear reconstructions of q . For this a gradient is estimated in each cell using nearby values (Sato et al., 2008) and limited to maintain positivity (Dukowicz and Kodis, 1987). The position at which the reconstructed value is evaluated is determined in a semi-Lagrangian fashion (Miura, 2007).

3 Dynamics

We now turn to the discretization of the momentum budget. A Hamiltonian formulation of the hydrostatic primitive equations in a generalized vertical coordinate is used (?). From this formulation the energy budget is obtained invoking only integration by parts, a structure easy to reproduce at the discrete level in order to conserve energy. Before arriving, at the end of this section, at the fully discrete three-dimensional equations, we start from the Hamiltonian of the hydrostatic primitive equations. Introducing a vertical discretization (of the Hamiltonian) produces (the Hamiltonian of) a compressible multi-layer Saint-Venant model. The Boussinesq approximation, enforced by a Lagrange multiplier, yields a standard multi-layer Saint-Venant model. Finally the horizontal discretization is described.

3.1 Continuous Hamiltonian

An ideal perfect gas with $p\alpha = RT$ and constant $C_p = R/\kappa$ is assumed where p is pressure, α specific volume and T temperature. Then

$$\begin{aligned}\pi &= C_p (p/p_r)^\kappa \\ \theta &= T (p/p_r)^{-\kappa} \\ \alpha &= \frac{RT}{p} = \frac{\kappa\theta\pi}{p},\end{aligned}$$

where π is the Exner function and θ potential temperature. Note that, letting $U(\alpha, \theta)$ be specific internal energy, $\partial U/\partial\alpha = -p$, $\partial U/\partial\theta = \pi$, $U + \alpha p - \theta\pi = 0$.

We work within the shallow-atmosphere and spherical geopotential approximation, so that gravity g is a constant, the elementary volume is $a^2 g^{-1} d\Phi d^2\mathbf{n}$ and $\dot{\mathbf{r}} \cdot \dot{\mathbf{r}} = g^{-2} \dot{\Phi}^2 + a^2 \mathbf{u} \cdot \mathbf{u}$. The primitive

equations are generated by the Hamiltonian :

$$H[\mu, \mathbf{v}, \Theta, \Phi] = \int_0^1 d\eta \left\langle \mu \left(a^2 \frac{\mathbf{u}(\mathbf{v}, \mathbf{n}) \cdot \mathbf{u}(\mathbf{v}, \mathbf{n})}{2} + U \left(\frac{1}{g\mu} \frac{\partial \Phi}{\partial \eta}, \frac{\Theta}{\mu} \right) + \Phi \right) \right\rangle \quad (12)$$

250 $+ p_\infty a^2 g^{-1} \langle \Phi(\eta = 1) \rangle$

where $\langle f(\mathbf{n}, \eta) \rangle = \int_\Sigma f d^2 \mathbf{n}$ with Σ the unit sphere and $\mathbf{v} = a^2 (\mathbf{u} + \mathbf{n} \times \boldsymbol{\Omega})$ is prognostic (Dubos and Tort, 2014). In (12) H is a functional of the three-dimensional fields $\mu, \mathbf{v}, \Theta, \Phi$ and $\mathbf{u}(\mathbf{v}, \mathbf{n}) = a^{-2} \mathbf{v} - \mathbf{n} \times \boldsymbol{\Omega}$. The terms in the integral are kinetic, internal and potential energy. The last term in (12) represents the work of pressure p_∞ exerted at the top $\eta = 1$ of the computational domain and

255 sets the upper boundary condition $p = p_\infty$.

Discretizing Hamiltonian (12) in the vertical direction yields a multi-layer Hamiltonian (Bokhove, 2002) :

$$H = \sum_k H_k [\mu_k, \mathbf{v}_k, \Theta_k, \Phi_{k+1/2}, \Phi_{k-1/2}] \quad (13)$$

$$+ p_\infty a^2 g^{-1} \int_\Sigma \Phi_N d^2 \mathbf{n}$$

260 $H_k = \left\langle \mu_k \left(a^2 \frac{\mathbf{u}(\mathbf{v}_k, \mathbf{n}) \cdot \mathbf{u}(\mathbf{v}_k, \mathbf{n})}{2} + U \left(\frac{\delta_k \Phi}{g\mu_k}, \frac{\Theta_k}{\mu_k} \right) + \bar{\Phi}^k \right) \right\rangle$

where $\mu_k = \int_{\eta_{k-1/2}}^{\eta_{k+1/2}} \mu d\eta$, $\Theta_k = \int_{\eta_{k-1/2}}^{\eta_{k+1/2}} \Theta d\eta$. Notice that μ_k, \mathbf{v}_k are at full model levels while geopotential Φ_l is placed at interfaces.

In order to reduce (13) to a multi-layer shallow-water system, the Boussinesq approximation is made by introducing into (13) Lagrange multipliers λ_k enforcing $\mu_k = a^2 \rho_r \frac{\delta_k \Phi}{g}$:

265 $H_k = \left\langle \mu_k \left(a^2 \frac{\mathbf{u}(\mathbf{v}_k) \cdot \mathbf{u}(\mathbf{v}_k)}{2} + (1 - \theta_k) \bar{\Phi}^k \right) + \lambda_k \left(\frac{\mu_k}{\rho_r} - a^2 \frac{\delta_k \Phi}{g} \right) \right\rangle + p_\infty a^2 g^{-1} \langle \Phi(\eta = \mathbb{1}) \rangle$

where θ_k is now the non-dimensional buoyancy of each layer. Notice that the last term can be omitted ($p_\infty = 0$). Indeed changing p_∞ only adds a constant to λ_{ik} and does not change the motion (see 3.3).

3.2 Fully discrete Hamiltonian

We now discretize horizontally the Hamiltonians (14,13,12). In addition to the kinematic degrees

270 of freedom μ_{ik}, Θ_{ik} we need to discretize the velocity degrees of freedom. Since we shall need the curl of \mathbf{v} , it is a 1-form in the nomenclature of discrete differentiation geometry. Hence we describe \mathbf{v} by the discrete integrals $v_{ek} = \int_{\Gamma_e} \mathbf{v}(\mathbf{n}, \eta_k) \cdot d\mathbf{l}$ (unit : m^2/s) where Γ_e is a triangular edge. An approximation of H is then given by :

$$H[\mu_{ik}, \Theta_{ik}, \Phi_{il}, v_{ek}] = K + P \quad (15)$$

275 $K = a^2 \sum_{ike} \mu_{ik} \frac{A_{ie}}{A_i} u_{ek}^2 \quad \text{where } u_{ek} = \frac{v_{ek} - R_e}{a^2 d_e},$

$$P = \sum_{ik} \mu_{ik} \left(\bar{\Phi}_i^k + U \left(\frac{a^2 A_i \delta_k \Phi_i}{g\mu_{ik}}, \frac{\Theta_{ik}}{\mu_{ik}} \right) \right) + p_\infty a^2 g^{-1} \sum_i A_i \Phi_{iL}$$

where $R_e = a^2 \int_{\Gamma_e} (\boldsymbol{\Omega} \times \mathbf{n}) \cdot d\mathbf{l}$ is the planetary contribution to v_e , d_e is the (angular) length of triangular edge Γ_e and A_{ie} is an (angular) area associated to edge Γ_e and to a cell i to which it belongs, with $A_{ie} = 0$ if Γ_e is not part of the boundary of cell i . u_{ek} is a first-order estimate of the component of \mathbf{u} along Γ_e . In planar geometry, $A_{ie} = \frac{1}{4} l_e d_e$ is a consistent formula for A_{ie} because it satisfies $A_i = \sum_e A_{ie}$ (Ringler et al., 2010). It is therefore also consistent in spherical geometry, with $A_i \simeq \sum_e A_{ie}$. Letting $A_{ie} = \frac{1}{4} l_e d_e$ simplifies somewhat the kinetic energy term :

$$K = \frac{a^2}{2} \sum_{ek} \left(\frac{\mu_k}{A} \right)^e l_e d_e u_{ek}^2 = \frac{a^2}{2} \sum_{ik} \frac{\mu_{ik}}{A_i} \overline{l_e d_e u_e^2}^i$$

Comparing (15) and (13) it is clear that (15) is also a valid horizontal discretization of (13). Regarding (14), a discretization of the kinetic energy part is simply K as above. The other terms are discretized in a straightforward way :

$$H = K + \sum_{ik} \left[\mu_{ik} \left(1 - \frac{\Theta_{ik}}{\mu_{ik}} \right) \overline{\Phi_i}^k + \lambda_{ik} \left(\frac{\mu_{ik}}{\rho_r} - a^2 A_i \frac{\delta_k \Phi_i}{g} \right) \right] + p_\infty a^2 g^{-1} \sum_i A_i \Phi_{iL} \quad (16)$$

with λ_{ik} the point-wise value of λ (0-form).

3.3 Discrete equations of motion

We now write the equations of motion corresponding to the discrete Hamiltonians. First mass fluxes must be computed for use by kinematics. It is computed as :

$$U_{ek} = \frac{\partial H}{\partial v_{ek}} = \left(\frac{\mu_k}{A} \right)^e l_e u_{ek}. \quad (17)$$

U_{ek} is therefore a centered estimate of the mass flux across the face orthogonal to edge Γ_e .

Next hydrostatic balance is expressed as $\partial H / \partial \Phi_{il} = 0$ or equivalently $H' = 0$ where H' is induced by arbitrary, independent variations of Φ only. For the compressible Hamiltonian (15) this yields

$$\begin{aligned} H' &= \sum_{ik} \left(\mu_{ik} \overline{\Phi_i}^k - \frac{a^2 A_i \delta_k \Phi_i}{g} p_{ik} \right) + p_\infty a^2 g^{-1} \sum_i A_i \Phi'_{iL} \\ &= \sum_{il} \left(\overline{\mu_i}^l + \frac{a^2 A_i}{g} \delta_l p_i \right) \Phi'_{il} + \sum_i \left(\frac{\mu_{iK}}{2} + \frac{a^2 A_i}{g} (p_\infty - p_{iK}) \right) \Phi'_{iL} \end{aligned}$$

Therefore $a^2 A_i \delta_l p_i + g \overline{\mu_i}^l = 0$ with the upper boundary condition $p_{iK} = p_\infty + g \mu_{iL} / (2a^2 A_i)$. These are discrete versions for $\partial_\eta p + \mu g = 0$ and $p(\eta = 1) = p_\infty$. p_{ik} can be determined starting from the top level. Alternatively one can define a pressure p_{il}^* at layer interfaces by $p_{iL}^* = p_\infty$ and $\delta_k p_i^* + g \mu_{ik} = 0$, then let $p_{ik} = \overline{p_i}^k$. Especially surface pressure is $p_i^s = p_\infty + g \sum_k \mu_{ik}$. When η is mass-based, one finds from (9) that $p_{il}^* = A_l p_i^s + C_l$ with surface pressure $p_i^s = p_\infty + g M_i$ and $C_l = g B_l + (1 - A_l) p_\infty$, i.e. the usual way to diagnose the vertical pressure profile from surface pressure is recovered. Once p_{ik} has been determined, the specific volume $\alpha_{ik} = \alpha(p_{ik}, \theta_{ik})$ follows. The geopotential is obtained by integrating :

$$\delta_k \Phi_i = \frac{g \mu_{ik} \alpha_{ik}}{a^2 A_i}, \quad \Phi_{i1/2} = \Phi_i^s, \quad (18)$$

starting from the ground, where Φ_i^s is the time-independent surface geopotential.

On the other hand for the incompressible Hamiltonian (16), geopotential Φ_{il} is obtained by enforcing the constraint $\partial H/\partial \lambda_{ik} = 0$, i.e. (18) but with specific volume $\alpha_{ik} = 1/\rho_r$ independent from pressure. Furthermore :

$$\begin{aligned} H' &= \sum_{ik} \left[(1 - \theta_{ik}) \mu_{ik} \overline{\Phi_i^k} - \lambda_{ik} a^2 A_i \frac{\delta_k \Phi_i'}{g} \right] + p_\infty a^2 g^{-1} \sum_i A_i \Phi'_{iL} \\ &= \sum_{il} \left(\frac{1}{(1 - \theta_i) \mu_i} + \frac{a^2 A_i}{g} \delta_l \lambda_i \right) \Phi'_{il} + \sum_i \left((1 - \theta_{iK}) \frac{\mu_{iK}}{2} - (p_\infty - \lambda_{ik}) a^2 g^{-1} A_i \right) \Phi'_{iL} \end{aligned}$$

Therefore λ_{ik} satisfies the same equations as p_{ik} but with $(1 - \theta_{ik}) \mu_{ik}$ instead of μ_{ik} , which shows that θ_{ik} acts indeed as a buoyancy $\theta = (\rho_r - \rho)/\rho_r$. The Lagrange multipliers λ_{ik} enforcing the incompressibility constraint are to be interpreted as the pressure at full model levels, a typical outcome within the Boussinesq approximation (Holm et al., 2002).

Finally the horizontal momentum balance is written in vector-invariant form. When $W = 0$:

$$\partial_t v_{ek} + \delta_e B_k + \theta_{ek}^* \delta_e \pi_k + (q_k U_k)_e^\perp = 0 \quad (19)$$

where

$$\pi_{ik} = \frac{\partial H}{\partial \Theta_{ik}}, \quad B_{ik} = \frac{\partial H}{\partial \mu_{ik}},$$

and the \perp operator is defined in Ringler et al. (2010) through antisymmetric weights $w_{ee'} = -w_{e'e}$:

$$(q_k U_k)_e^\perp = \sum_{e'} w_{ee'} q_{ee'} U_{e'} \quad \text{where } q_{ee'} = \frac{q_{e'k}^* + q_{ek}^*}{2}$$

with q_{ek}^* a value of potential vorticity reconstructed at e -points from values at v -points $q_{vk} = \delta_v v_k / \mu_v$, where μ_{vk} is μ integrated over triangular control volumes defined as an area-weighted sum of neighboring μ_{ik} (Ringler et al., 2010). Currently a centered average $q_{ek}^* = \overline{q_k}^e$ is used but other reconstructions, including upwind-biased reconstructions, could be used as well (Ringler et al., 2010). The weights $w_{ee'}$ are obtained by Thuburn et al. (2009), eq. 33 as a function of the ratios $R_{iv} = A_{iv}/A_i$ satisfying $\sum_v R_{iv} = 1$, i.e. $\sum_v A_{iv} = A_i$. Using the compressible Hamiltonian (15) one finds :

$$\pi_{ik} = \pi(\alpha_{ik}, \theta_{ik}), \quad (20)$$

$$B_{ik} = K_{ik} + \overline{\Phi_i^k}, \quad (21)$$

$$\text{where } K_{ik} = a^2 \frac{\overline{l_e d_e u_e^2}}{A_i} \quad (22)$$

is an approximation of kinetic energy $\frac{1}{2} a^2 \mathbf{u} \cdot \mathbf{u}$. Therefore geopotential at full levels is defined as a centered average of Φ_{il} and Exner pressure is diagnosed in each control volume using the equation of state. Because $p_{ik} = p(\alpha_{ik}, \theta_{ik})$, (20) simplifies to $\pi_{ik} = c_p (p_{ik}/p_r)^\kappa$. In practice π_{ik} and α_{ik} are both diagnosed from p_{ik}, θ_{ik} when solving the hydrostatic balance.

On the other hand using the incompressible Hamiltonian (16) yields

$$B_{ik} = K_{ik} + \overline{\Phi}_i^k + \frac{\lambda_{ik}}{\rho_r}, \quad \pi_{ik} = -\overline{\Phi}_{ik} \quad (23)$$

340 As already mentioned, changing p_∞ only modifies the upper boundary condition and only adds a constant to λ_{ik} . Since only $\delta_e B_k$ is important for dynamics, the value of p_∞ is arbitrary and can be set to 0. Now if $\theta_{ik} = \theta_k$ is horizontally uniform, $\theta_{ek}^* = \theta_k$ and :3.4

$$\delta_e B_k + \theta_{ek}^* \delta_e \pi_k = \delta_e \left(K_k + \frac{\lambda_k}{\rho_r} + (1 - \theta_k) \overline{\Phi}^k \right),$$

and (19) takes the expected form for a multi-layer shallow-water model. In the more general case 345 where θ_{ik} is not uniform, (19) is a discretization of the vector-invariant form of Ripa's equations (Ripa, 1993).

When $W \neq 0$ an additional term takes into account vertical momentum transport :

$$\begin{aligned} \partial_t v_{ek} + \delta_e B_k + \theta_{ek}^* \delta_e \pi_k + (q_k U_k)_e^\perp \\ + \left(\frac{\overline{W}^k}{\mu_k} \right)_e \delta_l v_e^* = 0 \end{aligned} \quad (24)$$

350 where v_{el}^* is a value of v_e reconstructed at interfaces. Here a centered average $v_{el}^* = \overline{v_e^l}$ is used. The above discretization does not possess particular conservation properties and other equally accurate formulae could be explored.

3.4 Time marching

After spatial discretization one obtains a large set of ordinary algebraic equations :

$$355 \quad \frac{\partial \mathbf{y}}{\partial t} = f(\mathbf{y}) \quad (25)$$

where $\mathbf{y} = (M_i, \Theta_{ik}, v_{ik})$ with a mass-based coordinate and $\mathbf{y} = (\mu_{ik}, \Theta_{ik}, v_{ik})$ with a Lagrangian coordinate. Geopotential Φ_{ik} is diagnosed from \mathbf{y} when computing the trends $f(\mathbf{y})$ (details below).

(25) is advanced in time using a scheme of Runge-Kutta type. **Temporal stability is limited by the external mode, which propagates at the speed of sound c . For a p -stage scheme, about $(p/C_{max}) \times$** 360 **$cT/\delta x$ evaluations of f are necessary to simulate a time T with resolution δx where C_{max} is the maximum time step allowed to integrate the differential equation $dx/dt = ix$. It is therefore desirable to maximize the effective Courant number $C_{eff} = C_{max}/p$. The design goals of the time scheme are to be fully explicit for simplicity, second-order accurate and with a favorable effective Courant number for efficiency.**

365 **2-stage Runge-Kutta schemes of order 2 are unconditionally unstable for imaginary eigenvalues and ruled out. All explicit p -step RK schemes of order p are equivalent for linear equations. $p = 3$ and $p = 4$ yield $C_{max}^{(3)} = \sqrt{3}$ and $C_{max}^{(4)} = 2\sqrt{2}$, respectively, hence $C_{eff}^{RK3} = 1/\sqrt{3} < C_{eff}^{RK4} = 1/\sqrt{2}$. Kinmark and Gray (1984b) provide p -stage Runge-Kutta schemes with optimal $C_{max} = p -$**

1 and order 2 for odd p (referred to as RK2.p below). Third- and fourth-order accuracy are achievable
 370 at a small price in terms of stability, i.e. $C_{max} = \sqrt{(p-1)^2 - 1}$ (Kinnmark and Gray, 1984a). Hence
 for $p = 4$ and $p = 5$ optimal schemes are *RK4* and *RK2.5*, the latter having $C_{eff} = 0.8$, about 13%
 larger than C_{eff}^{RK4} . Currently the following scheme $\mathbf{y}_n \mapsto \mathbf{y}_{n+1}$ is implemented for RK4 :

$$\begin{aligned} \mathbf{y}^1 &= \mathbf{y}_n + \frac{\tau}{4} f(\mathbf{y}_n) \\ \mathbf{y}^2 &= \mathbf{y}_n + \frac{\tau}{3} f(\mathbf{y}^1) \\ 375 \quad \mathbf{y}^3 &= \mathbf{y}_n + \frac{\tau}{2} f(\mathbf{y}^2) \\ \mathbf{y}_{n+1} &= \mathbf{y}_n + \tau f(\mathbf{y}^3), \end{aligned}$$

where $\tau \leq 2\sqrt{2}\delta x/c$ is the time step and $\mathbf{y}_n \simeq \mathbf{y}(n\tau)$. A similar sequence is used for RK2.5. This is
 a low-storage scheme since the same memory space can be used for $\mathbf{y}^1, \mathbf{y}^2, \mathbf{y}^3$ and \mathbf{y}_{n+1} . It is also
 very easy to implement. It is 4th order accurate for linear equations but only second-order accurate
 380 for non-linear equations.

Furthermore the last step is similar to an Euler step, hence

$$\delta_t \mu_{ik} + \delta_i (\tau U_k^3) + \delta_k (\tau W_i^3) = 0$$

so that the time-integrated mass fluxes expected by the transport scheme are simply $\overline{U}_{ek} = \tau U_{ek}^3, \overline{W}_{il} =$
 τW_{il}^3 or their sum over $N_{transport}$ successive time steps (see section 3).

385 **Recap : computation of trends in a mass coordinate**

At the beginning of this computation v_{ek}, M_i, Θ_{ik} are known. Cell-integrated mass μ_{ik} and potential
 temperature θ_{ik} are diagnosed using (9,8). Pressure p_{ik} follows from hydrostatic balance (see sub-
 section 3.3), then Exner pressure and specific volume π_{ik}, α_{ik} . Geopotential is obtained bottom-up
 using (18), then the Bernoulli function (21,22).

390 From μ_{ik}, v_{ek} horizontal mass fluxes U_{ek} are obtained then, by vertical integration, $\partial M_i / \partial t$. Then
 $\partial \mu_i / \partial t$ is obtained and injected into the mass budget (1) to compute the vertical mass flux W_{il}
 by a top-down integration. The potential temperature fluxes and trend are then computed using (7,8).
 Finally the velocity trend is computed following (24).

Recap : computation of trends in a Lagrangian coordinate

395 At the beginning of this computation $v_{ek}, \mu_{ik}, \Theta_{ik}$ are known. Potential temperature θ_{ik} is diagnosed
 using (9,8). Pressure p_{ik} (compressible equations) or λ_{ik} (incompressible equations) follows from
 hydrostatic balance (see subsection 3.3). Geopotential is obtained bottom-up using (18) and either
 $\alpha_{ik} = \alpha(\theta_{ik}, p_{ik})$ or $\alpha_{ik} = 1/\rho_r$, then the Bernoulli function and Exner pressure using either (21) or
 (23).

400 From μ_{ik}, v_{ek} horizontal mass fluxes U_{ek} is obtained then $\partial \mu_i / \partial t$. The trends of potential tem-
 perature and velocity are finally computed using (7) with $W_{il} = 0$ and (19).

3.5 Filters

Centered schemes need stabilization to counteract the generation of grid-scale features in the flow. Linear sources of grid-scale noise, e.g. dispersive numerical errors, may be handled by filters, e.g. upwinding or hyperviscosity. Other sources are genuinely non-linear, e.g. the downward cascade of energy or enstrophy. Here we handle these sources through hyperviscosity as well rather than with a proper turbulence model, e.g. Smagorinsky (1963), following a widespread although disputable practice (see Gassmann, 2013).

For this purpose hyper-diffusion is applied every N_{diff} time steps in a forward-Euler manner :

$$410 \quad \Theta_{ik} := \Theta_{ik} - N_{diff} \tau \frac{L_\theta^{2p}}{\tau_\theta} D_\theta^p \Theta_{ik} \quad (26)$$

$$v_{ek} := v_{ek} - N_{diff} \tau \left[\frac{L_\omega^{2p}}{\tau_\omega} D_\omega^p (v_{ek} - R_e) + \frac{L_\delta^{2p}}{\tau_\delta} D_\delta^p (v_{ek} - R_e) \right] \quad (27)$$

where the exponent p is 1 or 2, the dissipation time scales $\tau_\theta, \tau_\omega, \tau_\delta$ serve to adjust the strength of filtering, the length scales $L_\theta, L_\omega, L_\delta$ are such that $L_\theta^{-2}, L_\omega^{-2}, L_\delta^{-2}$ are the largest eigenvalue of the horizontal dissipation operators $D_\theta, D_\omega, D_\delta$ defined as :

$$415 \quad D_\theta \Theta_i = -\delta_i \left[\frac{l_e}{d_e} \delta_e \left(\frac{\Theta_i}{A_i} \right) \right]$$

$$D_\omega v_e = -\delta_e \left(\frac{1}{A_v} \delta_v v_e \right)$$

$$D_\delta v_e = -\delta_e \left(\frac{1}{A_i} \delta_i \left(\frac{l_e}{d_e} v_e \right) \right)$$

These positive definite operators correspond to diffusing a scalar, vorticity and divergence. Notice however than filtering with $p > 1$, although it damps grid-scale noise, does typically not remove entirely oscillations nor guarantee positivity of the filtered field (see e.g. Jiménez, 2006).

$L_\theta^{-2}, L_\omega^{-2}, L_\delta^{-2}$ are precomputed by applying $D_\theta, D_\omega, D_\delta$ many times in sequence on random data so that their largest eigenvalue is given by ratio of the norm of two successive iterates. This process converges very quickly and in practice 20 iterations are sufficient. The dissipation time scales and the exponents can be set to different values for θ, ω, δ . N_{diff} is determined as the largest integer that ensures stability, i.e. such that $N_{diff} \tau$ be smaller than all three dissipation time scales.

4 Energetics

4.1 Conservation and stability

In addition to its aesthetic appeal, discrete conservation of energy has practical consequences in terms of numerical stability which we discuss here using arguments similar to energy-Casimir stability theory (Arnold, 1965). Indeed if a dynamical system conserves a convex integral quantity, then any state of the system which is a minimum of that quantity is necessarily a stable steady-state.

For instance the states of rest of the shallow-water equations minimize a linear combination of total energy and mass. Each additional conserved integral quantity widens the family of steady states that can be proven to be stable. In the discussion below we assume that the discrete equations of motion
 435 conserve total energy. The additional conserved quantities then depend on the vertical coordinate used.

Assuming a Lagrangian vertical coordinate, the additional integral quantities conserved by the discrete equations of motion are, for each layer, the horizontally-integrated mass and potential temperature $\sum_i \mu_{ik}$, $\sum_i \Theta_{ik}$, which form a subset of the Casimir invariants of the continuous equations (Dubos and Tort, 2014). Stationary points of the pseudo-energy $H' = H - \sum_k \Phi_k \sum_i \mu_{ik} -$
 440 $\sum_k \pi_k \sum_i \Theta_{ik}$ are such that $\partial H / \partial v_{ek} = 0$ (state of rest), $\partial H / \partial \Theta_{ik} = \pi_{ik} = \pi_k$ and $\partial H / \partial \mu_{ik} = \overline{\Phi}_i^k = \Phi_k$. In the absence of topography, uniform $\overline{\Phi}_i^k$ and π_{ik} in each layer are achieved if θ_{ik} , μ_{ik} , Φ_{il} do not depend on the horizontal position i . Such states of rest are stable provided H' is convex.

The above reasoning shows that linearization of the discrete equations of motion around a steady
 445 state making H' convex yields linear evolution equations with purely imaginary eigenvalues. Forward integration in time is then linearly stable provided the relevant Courant-Friedrichs-Lewy condition is satisfied. Especially, it is not necessary for linear stability that the time-marching scheme conserves energy.

With a mass-based vertical coordinate, the exchange of mass between layers reduces the set of
 450 discrete Casimir invariants to total mass and potential temperature $\sum_i M_i$, $\sum_{ik} \Theta_{ik}$. Considering the linear combination $H' = H - \Phi \sum_i M_i - \pi \sum_{ik} \Theta_{ik}$ one finds the condition $\partial H / \partial \Theta_{ik} = \pi$. It is impossible to satisfy both hydrostatic balance and a uniform Exner pressure, hence no feasible state minimizes H' . On the other hand if cell-integrated entropy S_{ik} is prognosed instead of potential temperature, one can show that isothermal states of rest minimize $H' = H - \Phi \sum_i M_i - T \sum_{ik} S_{ik}$
 455 (Tort et al., 2014a).

We now proceed to derive the discrete energy budgets corresponding to a Lagrangian and a mass-based vertical coordinate. In these calculations only the adiabatic terms are considered, and the effect of the hyperviscous filters is omitted.

4.2 Lagrangian vertical coordinate

460 When $W = 0$ the continuous-time energy budget reads :

$$\begin{aligned} \frac{dH}{dt} &= \sum_{ik} \frac{\partial H}{\partial \lambda_{ik}} \partial_t \lambda_{ik} + \sum_{il} \frac{\partial H}{\partial \Phi_{il}} \partial_t \Phi_{il} + \sum_{ik} \frac{\partial H}{\partial \mu_{ik}} \partial_t \mu_{ik} + \sum_{ik} \frac{\partial H}{\partial \Theta_{ik}} \partial_t \Theta_{ik} + \sum_{ik} \frac{\partial H}{\partial v_{ek}} \partial_t v_{ek} \\ &= - \sum_{ik} \frac{\partial H}{\partial \mu_{ik}} \delta_i \frac{\partial H}{\partial v_{ek}} - \sum_{ik} \frac{\partial H}{\partial \Theta_{ik}} \delta_i \left(\theta_{ek}^* \frac{\partial H}{\partial v_{ek}} \right) \\ &\quad - \sum_{ek} \frac{\partial H}{\partial v_{ek}} \left(\delta_e \frac{\partial H}{\partial \mu_{ik}} + \theta_{ek}^* \delta_e \frac{\partial H}{\partial \Theta_{ik}} \right) - \sum_{ee'k} w_{ee'} q_{ee'}^* \frac{\partial H}{\partial v_{ek}} \frac{\partial H}{\partial v_{e'k}}. \end{aligned}$$

Using the discrete integration-by parts formula (4) and the antisymmetry property $w_{ee'} + w_{e'e} = 0$,
 465 one finds $dH/dt = 0$.

More generally, similar calculations yield the temporal evolution of an arbitrary quantity $F(\mu_{ik}, \Theta_{ik}, v_{ek}, \Phi_{il}, \lambda_{ik})$

:

$$\frac{dF}{dt} = \sum_{ik} \frac{\partial F}{\partial \lambda_{ik}} \partial_t \lambda_{ik} + \sum_{il} \frac{\partial F}{\partial \Phi_{il}} \partial_t \Phi_{il} + \{F, H\}_\mu + \{F, H\}_\Theta + \{F, H\}_v \quad (28)$$

$$\{F, H\}_\mu = \sum_{ek} \left(\frac{\partial H}{\partial v_{ek}} \delta_e \frac{\partial F}{\partial \mu_{ik}} - \frac{\partial F}{\partial v_{ek}} \delta_e \frac{\partial H}{\partial \mu_{ik}} \right) \quad (29)$$

$$470 \quad \{F, H\}_\Theta = \sum_{ek} \theta_{ek}^* \left(\frac{\partial H}{\partial v_{ek}} \delta_e \frac{\partial F}{\partial \Theta_{ik}} - \frac{\partial F}{\partial v_{ek}} \delta_e \frac{\partial H}{\partial \Theta_{ik}} \right) \quad (30)$$

$$\{F, H\}_v = - \sum_{ee'k} w_{ee'} q_{ee'}^* \frac{\partial F}{\partial v_{ek}} \frac{\partial H}{\partial v_{e'k}} \quad (31)$$

(28-31) imitate at the discrete level the Hamiltonian formulations obtained in Dubos and Tort (2014).

Discrete conservation of energy then appears as a consequence of the antisymmetry of the brackets

$\{F, H\}_\mu$, $\{F, H\}_\Theta$, $\{F, H\}_v$, the formulation of hydrostatic balance as $\partial H / \partial \Phi_{il} = 0$, and, in the

475 incompressible case, of the constraint $\partial H / \partial \lambda_{ik} = 0$. The antisymmetry of $\{F, H\}_\mu$, $\{F, H\}_\Theta$ is equivalent to the discrete integration-by-parts formula (4), itself equivalent to the discretization of the horizontal *div* and *grad* operators being compatible (see e.g. Taylor and Fournier 2010). The antisymmetry of $\{F, H\}_v$ results from $w_{ee'} = -w_{e'e}$ and $q_{ee'} = q_{e'e}$ (Ringler et al., 2010).

4.3 One-layer shallow-water equations

480 In the simplest case of a single layer without topography ($\Phi_s = 0$), the incompressible Hamiltonian (14) with $\Theta = 0$, $\rho_r = 1$, $a = 1$, $p_\infty = 0$ reduces to :

$$\begin{aligned} H &= \frac{1}{2} \sum_e \overline{\left(\frac{\mu}{A}\right)}^e l_e d_e u_{ek}^2 + \sum_i \left[\mu_i \frac{\Phi_i}{2} \right] \\ &= \frac{1}{2} \sum_e \bar{h}^e l_e d_e u_{ek}^2 + \frac{1}{2} \sum_i g A_i h_i^2 \end{aligned}$$

where $\Phi_i = gh_i$ is the geopotential at the ‘‘top’’ of the model and we have taken into account the

485 constraint $\mu_i = A_i h_i$, where h_i is interpreted as the thickness of the fluid layer. Hamiltonian H is precisely the one considered in Ringler et al. (2010). The discrete equations of motion also reduce to their energy-conserving scheme (not shown). (28) reduces to :

$$\frac{dF}{dt} = \{F, H\}_\mu + \{F, H\}_v \quad (32)$$

This is a discrete imitation of the shallow-water Poisson bracket. Had we used the enstrophy-

490 conserving scheme of Ringler et al. (2010) instead of the energy-conserving scheme, $\{F, H\}_v$ would have been :

$$\{F, H\}_v^Z = - \sum_{ee'k} w_{ee'} q_{e'k}^* \frac{\partial F}{\partial v_{ek}} \frac{\partial H}{\partial v_{e'k}} \quad (33)$$

This discrete bracket is not antisymmetric. Comparing (31) and (33) one sees that the energy-conserving bracket (31) is the antisymmetrization of (33), i.e. :

$$495 \quad \{F, H\}_v = \frac{1}{2} \left(\{F, H\}_v^Z - \{H, F\}_v^Z \right).$$

In the limit of the linearized shallow-water equations on the f -sphere Thuburn et al. (2009), both brackets (31-33) reduce to :

$$\{F, H\}_v^{lin} = -\frac{f}{\bar{h}} \sum_{ee'k} w_{ee'} \frac{\partial F}{\partial v_{ek}} \frac{\partial H}{\partial v_{e'k}} \quad (34)$$

where f is the constant value of the Coriolis parameter and \bar{h} is the background fluid layer thickness, 500 i.e. $h_e = \bar{h} + h'_e$, $h'_e \ll \bar{h}$.

In Ringler et al. (2010), the energy-conserving discretizations of the mass flux, kinetic energy and Coriolis term were devised by choosing a certain form and stencil for each of them with undetermined coefficients, deriving the energy budget, and choosing the undetermined coefficients in such a way that all contributions cancel out. In hindsight this delicate task could have been avoided by following the approach used here, inspired by Gassmann (2013) and advocated since some time already 505 by Salmon (Salmon, 1983, 2004): discretizing the energy and the brackets, instead of the equations of motion themselves. The critical part is to discretize the brackets. Starting from the linearized bracket (34) implicitly derived in Thuburn et al. (2009), a straightforward non-linear generalization is (33), which can be antisymmetrized to yield (31). From this point of view all the critical building blocks 510 of Ringler et al. (2010) were already obtained in Thuburn et al. (2009). The present approach generalizes this scheme to three-dimensional equations in a generalized vertical coordinate, exploiting recent advances in the relevant Hamiltonian formulation (?).

4.4 Mass-based vertical coordinate

When a mass-based coordinate is used instead of a Lagrangian vertical coordinate, additional terms 515 proportional to the vertical mass flux W_{il} appear in the equations of motion and in the energy budget. These terms cancel each other for the continuous equations but not necessarily for the discrete equations. It is possible to obtain a cancellation by imitating at the discrete level a relationship between the functional derivatives of H due to invariance under a vertical relabeling (remapping) (?). This strategy has been recently implemented in a longitude-latitude deep-atmosphere quasi-hydrostatic 520 dynamical core (Tort et al., 2014a). Tort et al. (2014a) estimate the numerical heat source due to the vertical transport terms as less than $10^{-3} W m^{-2}$ in idealized climate experiments (Held and Suarez, 1994). Hence canceling this very small numerical heat source is not yet implemented in DYNAMICO and energy is not exactly conserved when a mass-based vertical coordinate is used.

So far we see no indication that this would damage long-duration simulations (see numerical 525 results in section 5) but in the future strict energy conservation may be offered as an option, together with the choice to prognose entropy instead of potential temperature.

4.5 Relation with Gassmann (2013)

At this point some important differences with respect to the approach of Gassmann (2013) can be highlighted. Firstly, since the vertical coordinate is non-Eulerian, geopotential Φ depends on time and appears as an argument of the Hamiltonian. It therefore produces additional terms in the energy budget which vanish as shown in 4.2. On the other hand vertical momentum is not prognostic, since the equations are hydrostatic.

Secondly, Gassmann (2013) prognoses contravariant momentum components while we prognose v_{ek} , which are equivalent to covariant velocity components. Indeed the latter appear as the preferred prognostic variables in the Euler-Lagrange equations of motion (Tort and Dubos, 2014b) and their Hamiltonian formulation in a general vertical coordinate (Dubos and Tort, 2014). An immediate advantage of prognosing v_{ek} is that vorticity is trivially and naturally obtained along the lines of DEC. Furthermore the horizontal mass flux appears in the mass and tracer budgets through its contravariant components, and the functional derivatives of the Hamiltonian with respect to covariant momentum components are directly the contravariant mass flux components. This translates directly at the discrete level into (17). As a result the discrete Poisson bracket is almost trivial, with the exception of the Coriolis part. Hence averaging only occurs where it is unavoidable due to mesh staggering, i.e. in the discrete Coriolis term and in the Hamiltonian.

In a Eulerian formulation of the non-hydrostatic Euler equations, prognosing covariant components would have the drawback that the no-flux lower boundary condition involves a linear combination of all three covariant components, which on a staggered mesh may be difficult to discretize in an energy-conserving way. This may be a reason why Gassmann (2013) prognoses rather contravariant components. However with a mass-based or Lagrangian coordinate and hydrostatic equations, this is not an issue since the no-flux lower boundary condition only enters the mass budget.

550 5 Results

In this section, the correctness of DYNAMICO is checked using a few idealized test cases. Horizontal resolutions of $M = 32, 40, 64, 80, 128, 160$ are used. Defining mean horizontal resolution δx as the distance between hexagon centers on a regular planar hexagonal mesh covering the surface of the Earth with $10M^2$ cells, or equivalently the length of the edges of triangles in a regular triangular mesh with $20M^2$ triangles and the same surface, these values translate into $\delta x \simeq 280, 220, 140, 110, 70, 55 \text{ km}$.

Since our horizontal advection scheme is very similar to one scheme studied by Mittal and Skamarock (2010), we do not show two-dimensional results and focus on a three-dimensional test case of the DCMIP suite (Kent et al., 2014). Correctness of the three-dimensional dynamics solver is checked using the dry baroclinic instability setup of Jablonowski and Williamson (2006). Finally

M	Resolution	N_z	l_1	l_2	l_∞
40	220 km	30	0.7085	0.529	0.600
80	110 km	60	0.3136	0.285	0.4035
160	55 km	120	5.39×10^{-2}	7.01×10^{-2}	0.1705

Table 1: Global error norms for Hadley-like Meridional Circulation test case. Horizontal resolution is defined as $2R$ where $3\sqrt{3}/210M^2R^2 = 4\pi a^2$ is the radius of the $10M^2$ perfect and identical hexagons that would be needed to cover the surface $4\pi a^2$

the forced-dissipated setup defined by Held and Suarez (1994) is carried out to demonstrate the suitability of DYNAMICO for climate type simulations.

5.1 Transport by a prescribed Hadley-like Meridional Circulation

This test case consist of a single layer of tracer, which deforms over the duration of simulation.

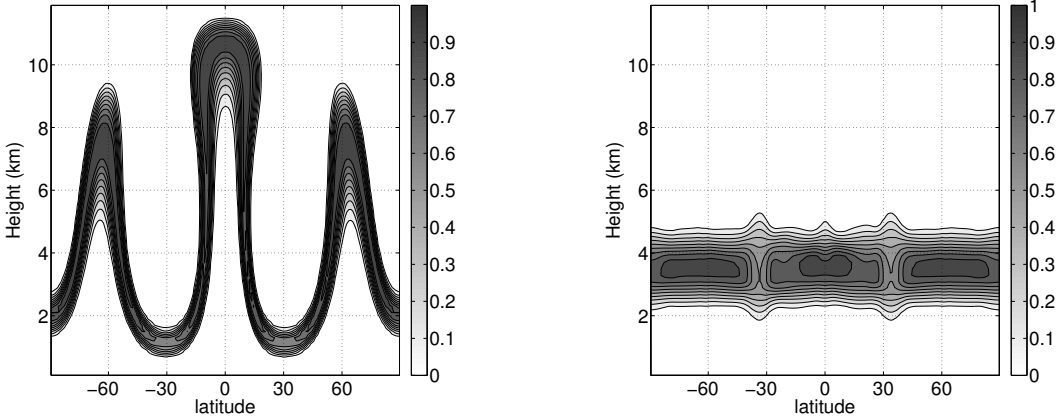
565 The flow field is prescribed so that the deformed filament returns to its initial position in the end of simulation. We used resolutions $M \times N_z = 40 \times 30, 80 \times 60, 160 \times 120$. The hybrid coefficients are computed so that the model levels are initially uniformly spaced. Figure 2 shows the tracer profile at $t = 12h$ and $t = 24h$ for horizontal resolutions $M = 80$ and $M = 160$. At $t = 24h$ the tracer field should ideally be independent of latitude, so any latitudinal dependance results from numerical errors. Figure 2(a,b) shows that for coarse resolution the scheme is diffusive and the final profile is quite diffused particularly at the downward bending points. Figure 2(c,d) shows that the increasing resolution decreases the diffusive nature of the advection scheme. Moreover the slope limiter successfully avoids the generation of spurious oscillations in the numerical solution. Table 1 shows the global error norms for different horizontal and vertical resolutions.

575 *As expected from two-dimensional test cases (Lauritzen et al., 2014a), our transport scheme is more diffusive than finite volume schemes on essentially Cartesian meshes such as those presented in Kent et al. (2014). Sample solutions (their Fig. 6) and error norms (their Table 6) they present indicate that our scheme achieves at resolution δx an accuracy similar to these schemes at resolution $2\delta x$.*

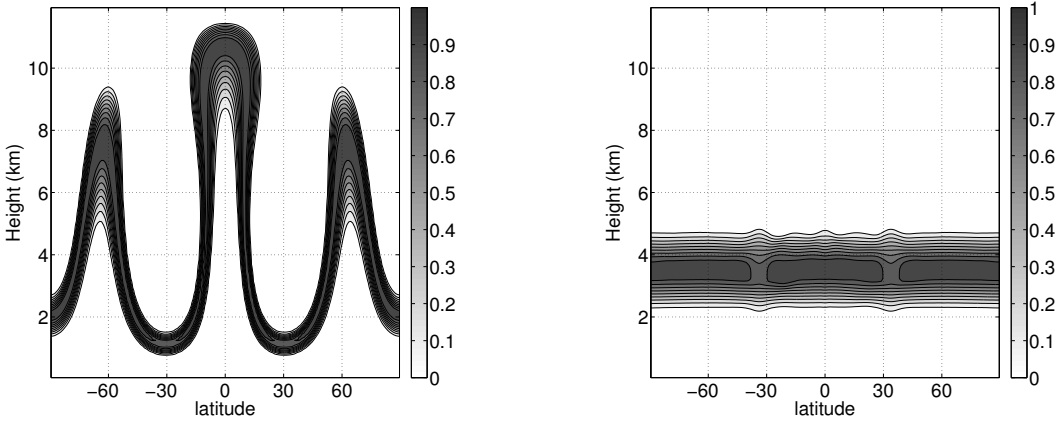
580

5.2 Baroclinic instability

The baroclinic instability benchmark of Jablonowski and Williamson (2006) is extensively used to test the response of 3D atmospheric models to a controlled, evolving instability. The initial state for this test case is the sum of a steady-state, baroclinically unstable, zonally-symmetric solution of the



(a) Horizontal resolution 110km ($M = 80$), 60 vertical levels.



(b) Horizontal resolution 55km ($M = 160$), 120 vertical levels.

Figure 2: Latitude-altitude plot of advected tracer profile at the mid time ($t = 12h$, left) and in the end of the simulation ($t = 24h$, right) for Hadley-like Meridional Circulation test case. Ideally, tracer isolines would be horizontal at the final time (contours separated by 0.1).

hydrostatic primitive equation and of a localized zonal wind perturbation triggering the instability in a deterministic and reproducible manner.

Even without the overlaid zonal wind perturbation, the initial state would not be perfectly zonally-symmetric because the icosahedral grid, as other quasi-uniform grids, is not zonally-symmetric.

590 Therefore the initial state possesses, in addition to the explicit perturbation, numerical deviations from zonal symmetry. This initial error, as well as truncation errors made at each time step by the numerical scheme, is not homogeneous but reflects the non-homogeneity of the grid. It nevertheless has the same symmetry as the grid, here wavenumber-5 symmetry. Due to the dynamical instability of the initial flow, the initial error is expected to trigger a wavenumber-5 mode of instability (provided

595 such an unstable mode with that zonal wavenumber exists). Depending on the amplitude of the initial truncation error, this mode can become visible, a case of grid imprinting (Lauritzen et al., 2010).

Fig. 3 presents results obtained at resolutions $M = 32, 64, 128$ (mean resolution 280, 140, 70 km) using 30 hybrid vertical levels and fourth-order filters ($p = 2$ in 26, 27). Dissipation time and time step are set to $\tau = 6h, 3h, 1.5h$ and $\delta t = 600s, 300s, 150s$ respectively. The right column shows the temperature field at pressure level $850hPa$ at day 9. At this day the baroclinic wave is well developed. The wave crest is reasonably sharp at $M = 32$, and becomes sharper at higher resolution. The simulated temperature field is qualitatively similar to those obtained at comparable resolutions by other models (e.g. Jablonowski and Williamson, 2006 Figs. 6, 7).

605 The left column shows surface pressure at day 12, after the baroclinic wave has broken, letting time for grid imprinting to develop. Grid imprinting in the Southern hemisphere, measured quantitatively as in Lauritzen et al. (2010) as the root-mean-square departure of surface pressure from its unperturbed value of $1000hPa$, exceeds $0.5hPa$ at day 9 at $M = 32$, at day 11 at $M = 64$ and at day 13 at $M = 128$. Comparing with Fig. 12 of Lauritzen et al. (2010), these values are in the low end of icosahedral models.

610

5.3 Thermally-forced idealized general circulation

Held and Suarez (1994) propose a benchmark to evaluate the statistically steady states produced by the dynamical cores used in climate models. Detailed radiative, turbulence and moist convective parametrization are replaced with very simple forcing and dissipation. The simple forcing and dissipation are designed in terms of a simple relaxation of the temperature field to a zonally-symmetric state and Rayleigh damping of low-level winds to represent the boundary-layer friction. We use 19 hybrid vertical levels and fourth-order filters ($p = 2$ in 26, 27) at resolutions 280 km and 140 km ($M = 32, 64$). Statistics are computed over the last 1000 days excluding initial 200 days, left for spin-up time of the model. Temporal statistics are computed from daily samples on the native grid at constant model level, then interpolated to a lat-lon mesh and zonally-averaged.

620 Figure 4 presents statistics obtained when using horizontal resolution of 280 km ($M = 32$) and dissipation time $\tau = 6h$. The model is stable for longer dissipation times ($\tau = 24h$) but smaller values produce smoother fields. Statistics obtained at resolution 140 km ($M = 64$) with $\tau = 3h$ are presented in Fig. 5. First-order statistics (panels ab) are close to those presented in Held and Suarez (1994) and present very little sensitivity to resolution. Second-order statistics are slightly more sensitive to resolution and increase slightly from $M = 32$ to $M = 64$. Temperature variance at $M = 64$ is close to that presented in Held and Suarez (1994) and slightly smaller than that obtained by Wan et al. (2013) on a triangular icosahedral grid at comparable resolution R2B5.

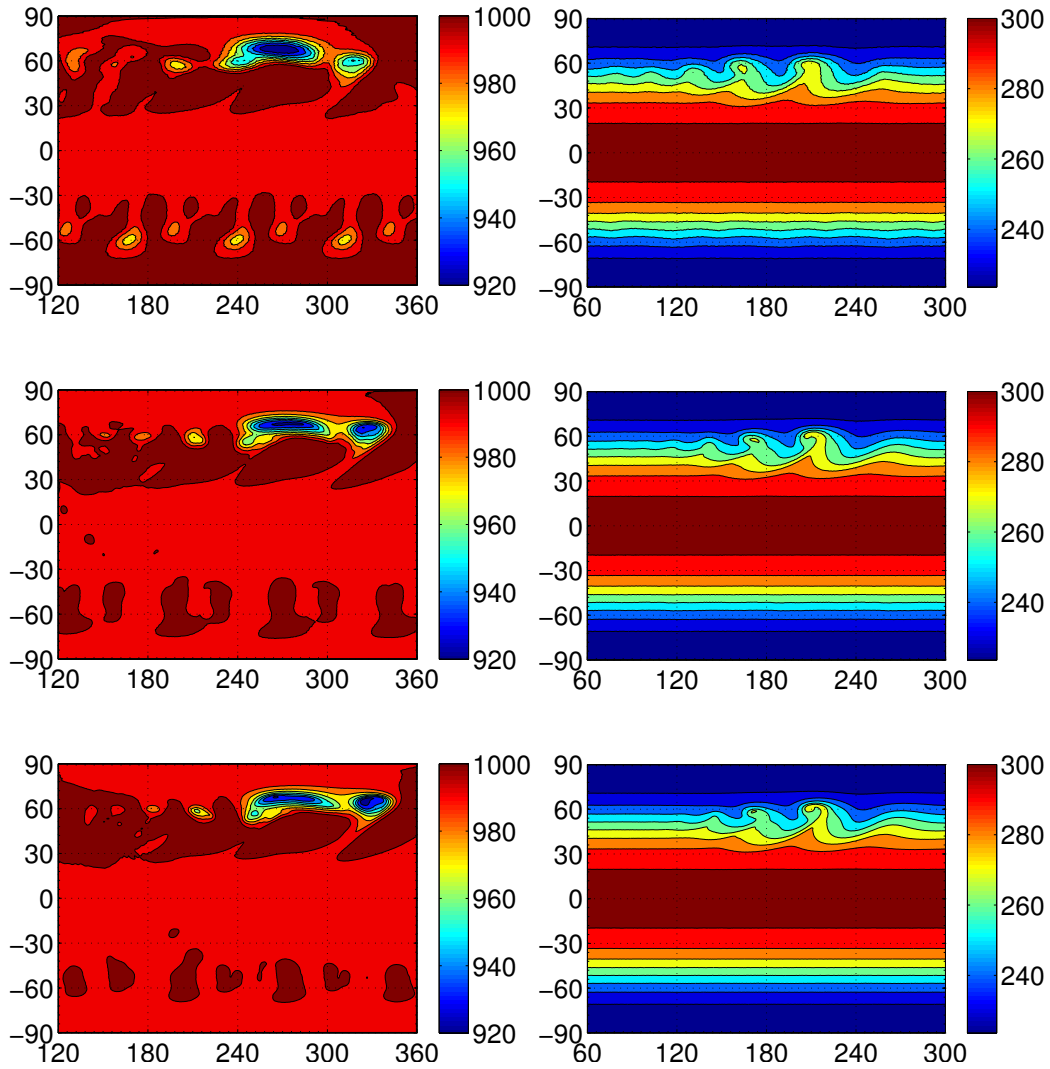


Figure 3: Dry baroclinic instability test case (Jablonowski and Williamson, 2006). Left : surface pressure in hPa at day 12 (contours separated by $10hPa$). Right : temperature in K at day 9 (contours separated by $10K$) and $850hPa$. Resolution increases from top to bottom rows : $280km$, $M = 32$ (top), $140km$, $M = 64$ (middle), $70km$, $M = 128$ (bottom).

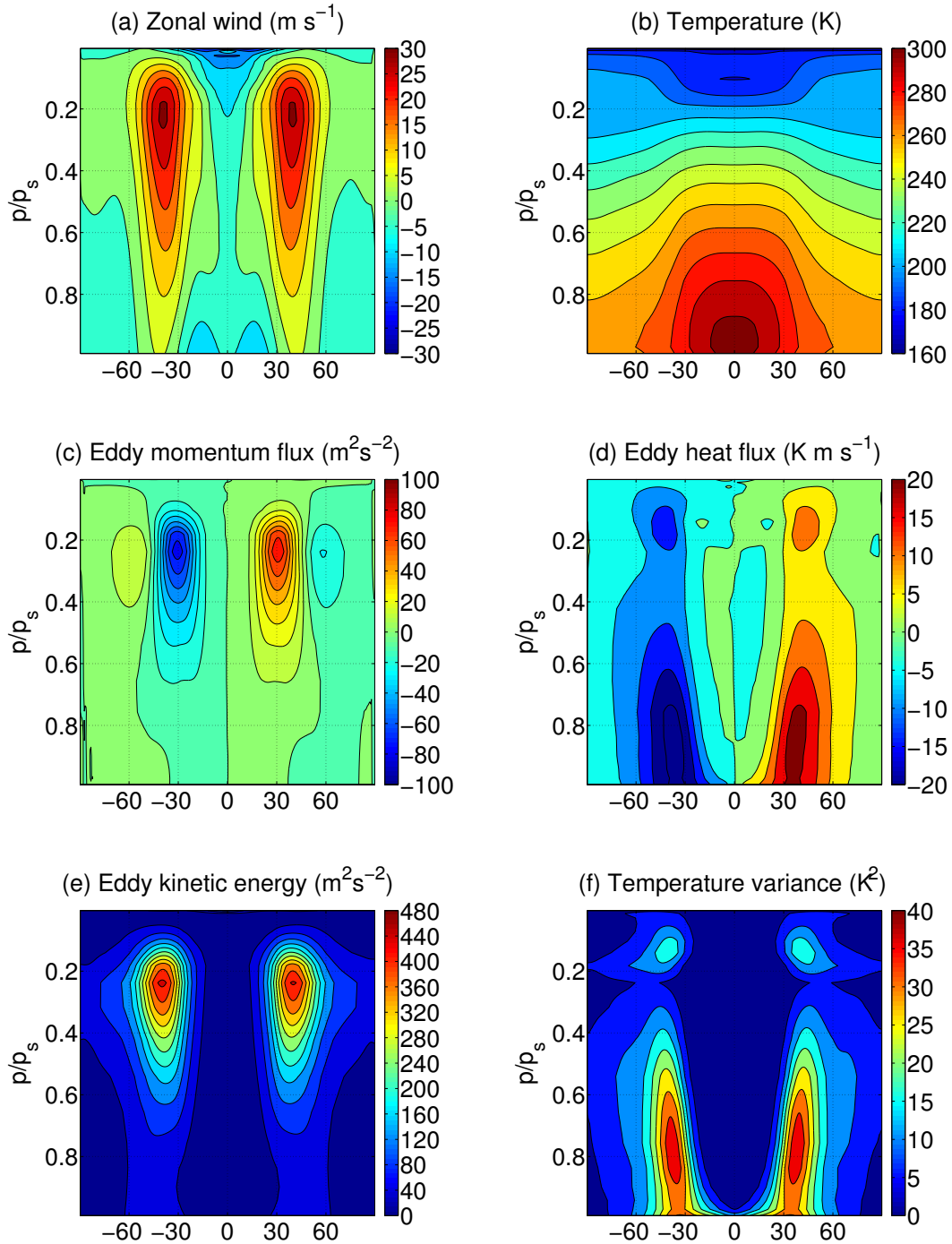


Figure 4: Time-zonal statistics of Held and Suarez (1994) experiment at resolution $280 km$ ($M = 32$) with dissipation time $\tau = 6h$. Contour intervals are $5 m s^{-1}$ (zonal wind), $10 K$ (temperature), $20 m^2 s^{-2}$ (eddy momentum flux), $5 K m s^{-1}$ (eddy heat flux), $40 m^2 s^{-2}$ (eddy kinetic energy) and $5 K^2$ (temperature variance).

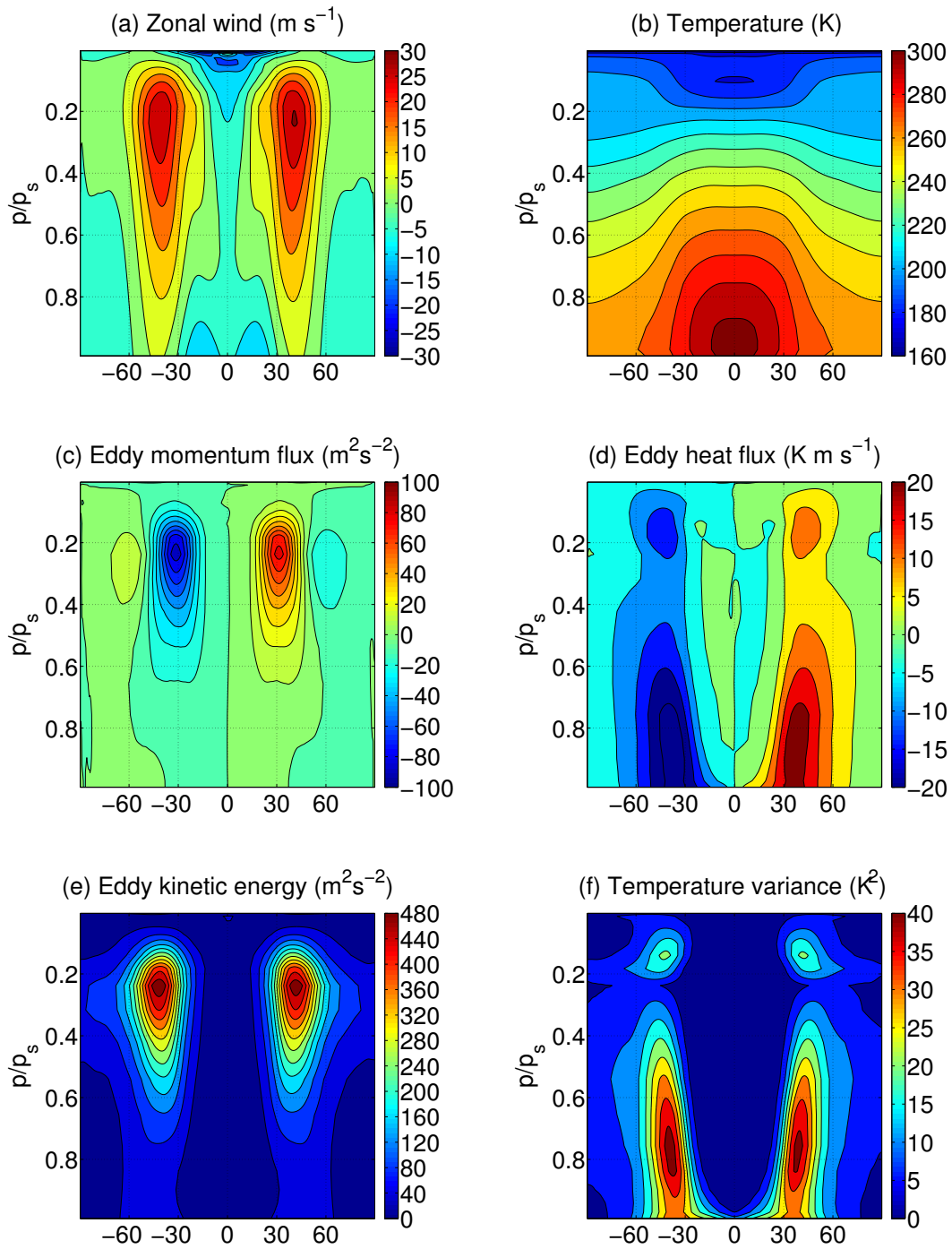


Figure 5: Time-zonal statistics of Held and Suarez (1994) experiment at resolution 140 km ($M = 64$) with dissipation time $\tau = 3h$. Contour intervals as in Fig. 4.

6 Conclusions

630 6.1 Contributions

A number of building blocks of DYNAMICO are either directly found in the literature or are adaptations of standard methods : explicit Runge-Kutta time stepping, mimetic horizontal finite-difference operators (Bonaventura and Ringler, 2005; Thuburn et al., 2009; Ringler et al., 2010), piecewise-linear slope-limited finite-volume reconstruction (Dukowicz and Kodis, 1987; Tomita et al., 2001),
635 swept-area calculation of scalar fluxes (Miura, 2007), directionally-split time integration of three-dimensional transport (e.g.Hourdin and Armengaud, 1999). It is therefore useful to highlight the two specific contributions brought forward, in our opinion, in the design of DYNAMICO, and that can be of broader applicability for model design.

640 The first contribution is to separate kinematics from dynamics as strictly as possible. This separation means that the transport equations for mass, scalars and entropy use no information regarding the specific momentum equation being solved. This includes the equation of state as well as any metric information, which is factored into the prognosed degrees of freedom and into the quantities derived from them (especially the mass flux). Metric information is not used to prognose tracer, mass and
645 potential temperature. It is confined in a few operations computing the mass flux, Bernoulli function and Exner function from the prognostic variables. This formulation is in line with more general lines of thought known as physics-preserving discretizations (Koren et al., 2014) and discrete differential geometry (Thuburn and Cotter, 2012). **Similarly, while we use the exact same hybrid vertical coordinate as most hydrostatic primitive equations model, we insist that it should be considered as mass-**
650 **based rather than pressure-based. Indeed the coincidence (up to time-independent multiplicative and additive factors) of mass and pressure is a peculiarity of the traditional shallow-atmosphere hydrostatic equations with a pressure top boundary condition. Recognizing the fundamentally kinematic definition of the hybrid coordinate in terms of mass rather than pressure emphasizes its relevance for solving other equation sets, especially non-hydrostatic (Laprise, 1992).**

655 The second contribution is to combine this kinematics-dynamics separation with a Hamiltonian formulation of the equations of motion to achieve energetic consistency. This approach extends the work of Gassmann (2013) to hydrostatic equations of motion and non-Eulerian vertical coordinates. This extension relies itself on a recent corresponding extension of the Hamiltonian theory of atmospheric fluid motion (Tort and Dubos, 2014b; Dubos and Tort, 2014). The Hamiltonian approach
660 further confines the equation-dependent parts of the numerical scheme to a single quantity, the total energy of the system expressed in terms of the prognostic variables and, in the case of hydrostatic equations, geopotential. The latter is a pseudo-prognostic variable which is an argument of the Hamiltonian but is diagnosed at each time step by enforcing the hydrostatic constraint, found to be simply the condition that the derivatives of the Hamiltonian with respect to geopotential degrees of

665 freedom vanish. This variational formulation of hydrostatic balance was first identified in the context
of the deep-atmosphere quasi-hydrostatic equations (Tort et al., 2014a) then generalized (Dubos and
Tort, 2014) and applied to DYNAMICO within the shallow-atmosphere approximation. Ultimately
the choice of a specific equation set boils down to choosing and discretizing the Hamiltonian, with-
out changing the general structure of the algorithm computing the tendencies.

670

These two advances yield our design goals, consistency and versatility. The desired ability to solve
different equation sets is currently limited to the hydrostatic primitive equations and the multi-layer
Saint-Venant or Ripa equations, but little work is required to solve other similar equations like the
recently derived non-traditional spherical shallow-water equations (Tort et al., 2014b). Whichever
675 set of equations needs to be solved in the future, including the fully compressible Euler equations,
energetic consistency is guaranteed if the general approach followed here and in Tort et al. (2014a)
is applied. Furthermore this approach is not limited to finite-difference schemes but can be extended
to finite element schemes.

We would also like to emphasize what the Hamiltonian approach does *not* achieve. Good numer-
680 ical dispersion crucially depends on grid staggering (for finite differences) or on the finite element
spaces used to represent the various quantities. It is entirely possible to design an energy-conserving
schemes with disastrous numerical dispersion properties. Other properties, such as exact geostrophic
equilibria or a discrete potential vorticity budget, come in addition to the antisymmetry of the dis-
crete Poisson bracket, as discussed in section 4 (see also Cotter and Thuburn, 2014). However the
685 Hamiltonian formulation provides a divide-and-conquer strategy by allowing to easily transfer these
additional properties to new sets of equations once they have been obtained for a specific one.

6.2 Outlook for DYNAMICO

A Lagrangian vertical coordinate is currently available as an option. In the absence of the vertical
remapping that must necessarily take place occasionally in order to prevent Lagrangian surfaces to
690 fold or cross each other, this option can not be used over meaningful time intervals. However it is con-
venient for development purposes since it allows to investigate separately issues related to the vertical
and horizontal discretizations. Nevertheless a future implementation of vertical remapping would be
a useful addition. There is room for improvement on other points. Especially it may be worth im-
proving the accuracy of the transport scheme, especially for water vapor and other chemically or
695 radiatively active species. Regarding potential temperature, Skamarock and Gassmann (2011) have
found that a third- order transport scheme for the potential temperature could significantly reduce
phase errors in the propagation of baroclinic waves. Whether more accurate transport of potential
temperature is beneficial for climate modelling remains to be determined.

The Hamiltonian framework leaves a complete freedom with respect to the choice of a discrete
700 Hamiltonian. Here the simplest possible second-order accurate approximation is used, but other

forms may yield additional properties, such as a more accurate computation of the geopotential. Ongoing work suggests that it is possible to design a Hamiltonian such that certain hydrostatic equilibria are exactly preserved in the presence of arbitrary topography. Such a property is sometimes achieved by finite-volume schemes (Botta et al., 2004; Audusse et al., 2004), and its absence is one
705 manifestation of the so-called pressure-gradient force error (Gary, 1973).

DYNAMICO is stabilized by (bi)harmonic operators to which we refer as filters rather than dissipation. Indeed they are numerical devices aimed at stabilizing the model rather than physically-based turbulence models such as nonlinear viscosity (Smagorinsky, 1963). Turbulence models induce a well-defined dissipation rate of resolved kinetic energy that should enter as a positive source term in
710 the entropy budget in order to close the energy budget. Emulating this process in a discrete model can however prove difficult (Gassmann, 2013). Indeed, in order to convert into heat the kinetic energy destroyed by filters, one needs to recast their contribution to the energy budget as a positive definite sum. Whether this can be done in DYNAMICO is left for future investigation.

Coupling DYNAMICO to the LMD-Z terrestrial physics package suite is ongoing. For planetary
715 applications, it will be important to also check the discrete angular momentum budget (Lebonnois et al., 2012; Lauritzen et al., 2014b).

In the near future DYNAMICO should become able to solve richer, quasi-hydrostatic equations (White and Bromley, 1995; Tort and Dubos, 2014a) and to take into account deviations of the geopotential from spherical geometry (Tort and Dubos, 2014b). Extension to fully-compressible Euler
720 equations is the next step and should leave its general structure unchanged (Dubos and Tort, 2014).

Code availability

Results presented in this article are based on **release r339** of DYNAMICO. Instructions to download, compile, and run the code are provided at <http://forge.ipsl.jussieu.fr/dynamico/wiki>. DYNAMICO is licensed under the terms of the CeCILL open source license.

Acknowledgements

The authors would like to thank two anonymous referees for their detailed and constructive criticism. S.D. has benefitted from the support of the Indo-French Centre for the Promotion of Advanced Research (IFCPRA/CEFIPRA) under the sponsored project number 4107-1. T.D., Y.M. and F.H. acknowledge the support of the French Agence Nationale de la Recherche (ANR) under reference
730 ANR-14-CE23-0010-01.

References

- A. Arakawa. Computational design for long-term numerical integration of the equations of fluid motion: Two-dimensional incompressible flow. Part I. *J. Comput. Phys*, 1(1):119–143, 1966.
- 735 Akio Arakawa and Vivian R. Lamb. A potential enstrophy and energy conserving scheme for the shallow water equations. *Mon. Wea. Rev.*, 109(1):18–36, January 1981.
- V. I. Arnold. Conditions for non-linear stability of plane steady curvilinear flows of an ideal fluid. *Doklady Akademii Nauk Sssr*, 162(5):773–777, 1965.
- Emmanuel Audusse, François Bouchut, Marie-Odile Bristeau, Rupert Klein, and Benoît Perthame. A fast and stable Well-Balanced scheme with hydrostatic reconstruction for shallow water flows. *SIAM Journal on*
740 *Scientific Computing*, 25(6):2050–2065, January 2004. ISSN 1064-8275.
- Jeffrey M. Augenbaum and Charles S. Peskin. On the construction of the voronoi mesh on a sphere. *J. Comput. Phys*, 59(2):177–192, June 1985. ISSN 00219991.
- O. Bokhove. Eulerian variational principles for stratified hydrostatic equations. *J. Atmos. Sci*, 59(9):1619–1628, May 2002.
- 745 Luca Bonaventura and Todd Ringler. Analysis of discrete Shallow-Water models on geodesic delaunay grids with C-Type staggering. *Mon. Wea. Rev.*, 133(8):2351–2373, August 2005.
- N. Botta, R. Klein, S. Langenberg, and S. Lützenkirchen. Well balanced finite volume methods for nearly hydrostatic flows. *J. Comput. Phys*, 196(2):539–565, May 2004. ISSN 00219991.
- C. J. Cotter and J. Thuburn. A finite element exterior calculus framework for the rotating shallow-water equations. *J. Comput. Phys*, 257:1506–1526, January 2014. ISSN 00219991.
750
- Qiang Du, Vance Faber, and Max Gunzburger. Centroidal voronoi tessellations: Applications and algorithms. *SIAM Review*, 41(4):637–676, 1999. ISSN 00361445.
- Qiang Du, Maria Emelianenko, and Lili Ju. Convergence of the lloyd algorithm for computing centroidal voronoi tessellations. *SIAM Journal on Numerical Analysis*, 44(1):102–119, January 2006. ISSN 1095-
755 7170.
- S. Dubey, T. Dubos, F. Hourdin, and H. C. Upadhyaya. On the inter-comparison of two tracer transport schemes on icosahedral grids. *Applied Mathematical Modelling*, April 2015. ISSN 0307904X.
- Thomas Dubos and Marine Tort. Equations of atmospheric motion in Non-Eulerian vertical coordinates: Vector-Invariant form and Quasi-Hamiltonian formulation. *Mon. Wea. Rev.*, 142(10):3860–3880, July 2014.
- 760 John K. Dukowicz and John W. Kodis. Accurate conservative remapping (rezoning) for arbitrary Lagrangian-Eulerian computations. *SIAM Journal on Scientific and Statistical Computing*, 8(3):305–321, May 1987. ISSN 2168-3417.
- Richard C. Easter. Two modified versions of bott’s Positive-Definite numerical advection scheme. *Mon. Wea. Rev.*, 121(1):297–304, January 1993. ISSN 1520-0493.
- 765 John M. Gary. Estimate of truncation error in transformed coordinate, primitive equation atmospheric models. *J. Atmos. Sci.*, 30(2):223–233, March 1973. ISSN 1520-0469.
- Almut Gassmann. Inspection of hexagonal and triangular c-grid discretizations of the shallow water equations. *J. Comput. Phys*, 230(7):2706–2721, April 2011. ISSN 00219991.
- Almut Gassmann. A global hexagonal c-grid non-hydrostatic dynamical core (ICON-IAP) designed for energetic consistency. *Quat. J. Roy. Met. Soc.*, 139(670):152–175, January 2013. ISSN 0035-9009.
770

- Isaac M. Held and Max J. Suarez. A proposal for the intercomparison of the dynamical cores of atmospheric general circulation models. *Bull. Am. Meteorol. Soc.*, 75(10):1825–1830, October 1994. ISSN 1520-0477.
- Darryl D. Holm, Jerrold E. Marsden, and Tudor S. Ratiu. *The Euler-Poincaré Equations in Geophysical Fluid Dynamics*, pages 251–299. Cambridge University Press, Cambridge, 2002.
- 775 F. Hourdin. Transport de l'énergie dans le modèle du LMD. *internal report, IPSL*, 1994.
- Frédéric Hourdin and Alexandre Armengaud. The use of finite-volume methods for atmospheric advection of trace species. Part I: Test of various formulations in a general circulation model. *Mon. Wea. Rev.*, 127(5): 822–837, May 1999.
- Frédéric Hourdin, Jean-Yves Grandpeix, Catherine Rio, Sandrine Bony, Arnaud Jam, Frédérique Cheruy, Nicolas Rochetin, Laurent Fairhead, Abderrahmane Idelkadi, Ionela Musat, Jean-Louis Dufresne, Alain Lahellec, Marie-Pierre Lefebvre, and Romain Roehrig. LMDZ5B: the atmospheric component of the IPSL climate model with revisited parameterizations for clouds and convection. *Clim. Dyn.*, 40(9-10):2193–2222, April 2013. ISSN 0930-7575.
- 780 Christiane Jablonowski and David L. Williamson. A baroclinic instability test case for atmospheric model dynamical cores. *Quarterly Journal of the Royal Meteorological Society*, 132(621C):2943–2975, October 2006. ISSN 00359009.
- Javier Jiménez. Hyperviscous vortices. *J. Fluid Mech.*, 279(-1):169–176, April 2006. ISSN 1469-7645.
- James Kent, Paul A. Ullrich, and Christiane Jablonowski. Dynamical core model intercomparison project: Tracer transport test cases. *Quat. J. Roy. Met. Soc.*, 140(681):1279–1293, April 2014. ISSN 00359009.
- 790 Ingemar P. Kinnmark and William G. Gray. One step integration methods of third-fourth order accuracy with large hyperbolic stability limits. *Mathematics and Computers in Simulation*, 26(3):181–188, June 1984a. ISSN 0378-4754.
- Ingemar P. E. Kinnmark and William G. Gray. One step integration methods with maximum stability regions. *Mathematics and Computers in Simulation*, 26(2):87–92, April 1984b. ISSN 03784754.
- 795 Barry Koren, Rémi Abgrall, Pavel Bochev, Jason Frank, and Blair Perot. Physics-compatible numerical methods. *J. Comput. Phys*, 257:1039+, January 2014. ISSN 00219991.
- René Laprise. The euler equations of motion with hydrostatic pressure as an independent variable. *Mon. Wea. Rev.*, 120(1):197–207, January 1992.
- P. H. Lauritzen, W. C. Skamarock, M. J. Prather, and M. A. Taylor. A standard test case suite for two-dimensional linear transport on the sphere. *Geoscientific Model Development Discussions*, 5(1):189–228, January 2012.
- 800 P. H. Lauritzen, P. A. Ullrich, C. Jablonowski, P. A. Bosler, D. Calhoun, A. J. Conley, T. Enomoto, L. Dong, S. Dubey, O. Guba, A. B. Hansen, E. Kaas, J. Kent, J. F. Lamarque, M. J. Prather, D. Reinert, V. V. Shashkin, W. C. Skamarock, B. Sørensen, M. A. Taylor, and M. A. Tolstykh. A standard test case suite for two-dimensional linear transport on the sphere: results from a collection of state-of-the-art schemes. *Geosci. Mod. Dev.*, 7(1):105–145, January 2014a.
- 805 Peter H. Lauritzen, Christiane Jablonowski, Mark A. Taylor, and Ramachandran D. Nair. Rotated versions of the jablonowski Steady-State and baroclinic wave test cases: A dynamical core intercomparison. *J. Adv. Model. Earth Syst.*, 2(4):15+, April 2010. ISSN 1942-2466.

- 810 Peter H. Lauritzen, Julio T. Bacmeister, Thomas Dubos, Sébastien Lebonnois, and Mark A. Taylor. Held-Suarez simulations with the community atmosphere model spectral element (CAM-SE) dynamical core: A global axial angular momentum analysis using eulerian and floating lagrangian vertical coordinates. *J. Adv. Model. Earth Syst.*, 6(1):129–140, March 2014b.
- Sébastien Lebonnois, Frédéric Hourdin, Vincent Eymet, Audrey Crespin, Richard Fournier, and François Forget. Superrotation of venus’ atmosphere analyzed with a full general circulation model. *J. Geophys. Res.*, 115:E06006+, June 2010. ISSN 0148-0227.
- 815 Sébastien Lebonnois, Curt Covey, Allen Grossman, Helen Parish, Gerald Schubert, Richard Walterscheid, Peter Lauritzen, and Christiane Jablonowski. Angular momentum budget in general circulation models of superrotating atmospheres: A critical diagnostic. *J. Geophys. Res.*, 117(E12):n/a, December 2012. ISSN 01480227.
- 820 Rashmi Mittal and William C. Skamarock. Monotonic limiters for a Second-Order Finite-Volume advection scheme using Icosahedral-Hexagonal meshes. *Mon. Wea. Rev.*, 138(12):4523–4527, August 2010.
- Hiroaki Miura. An Upwind-Biased conservative advection scheme for spherical Hexagonal-Pentagonal grids. *Mon. Wea. Rev.*, 135(12):4038–4044, December 2007.
- Hiroaki Miura and Masahide Kimoto. A comparison of grid quality of optimized spherical Hexagonal-Pentagonal geodesic grids. *Mon. Wea. Rev.*, 133(10):2817–2833, October 2005.
- 825 T. D. Ringler, J. Thuburn, J. B. Klemp, and W. C. Skamarock. A unified approach to energy conservation and potential vorticity dynamics for arbitrarily-structured c-grids. *J. Comput. Phys.*, 229(9):3065–3090, May 2010. ISSN 00219991.
- P. Ripa. Conservation laws for primitive equations models with inhomogeneous layers. *Geophys. Astrophys. Fluid Dyn.*, 70(1-4):85–111, June 1993.
- 830 P. Rípodas, A. Gassmann, J. Förstner, D. Majewski, M. Giorgetta, P. Korn, L. Kornblueh, H. Wan, G. Zängl, L. Bonaventura, and T. Heinze. Icosahedral Shallow Water Model (icoswm): results of shallow water test cases and sensitivity to model parameters. *Geosci. Mod. Dev.*, 2(2):231–251, December 2009.
- R. Sadourny. Compressible model flows on the sphere. *J. Atmos. Sci.*, 32(11):2103–2110, November 1975a.
- 835 Robert Sadourny. Conservative Finite-Difference approximations of the primitive equations on Quasi-Uniform spherical grids. *Mon. Wea. Rev.*, 100(2):136–144, February 1972.
- Robert Sadourny. The dynamics of Finite-Difference models of the Shallow-Water equations. *J. Atmos. Sci.*, 32(4):680–689, April 1975b.
- Robert Sadourny, A. K. I. O. Arakawa, and Y. A. L. E. Mintz. Integration of the nondivergent barotropic vorticity equation with an icosahedral-hexagonal grid for the sphere1. *Mon. Wea. Rev.*, 96(6):351–356, June 1968.
- 840 Rick Salmon. Practical use of hamilton’s principle. *J. Fluid Mech.*, 132:431–444, 1983.
- Rick Salmon. Poisson-Bracket approach to the construction of energy- and Potential-Enstrophy-conserving algorithms for the Shallow-Water equations. *J. Atmos. Sci.*, 61(16):2016–2036, August 2004.
- 845 M. Satoh, T. Matsuno, H. Tomita, H. Miura, T. Nasuno, and S. Iga. Nonhydrostatic icosahedral atmospheric model (NICAM) for global cloud resolving simulations. *Journal of Computational Physics*, 227(7):3486–3514, March 2008.
- A. J. Simmons and D. M. Burridge. An energy and Angular-Momentum conserving vertical Finite-Difference scheme and hybrid vertical coordinates. *Monthly Weather Review*, 109(4):758–766, April 1981.

- 850 William C. Skamarock and Almut Gassmann. Conservative transport schemes for spherical geodesic grids: High-Order flux operators for ODE-based time integration. *Mon. Wea. Rev.*, 139(9):2962–2975, April 2011.
- William C. Skamarock, Joseph B. Klemp, Michael G. Duda, Laura D. Fowler, Sang-Hun Park, and Todd D. Ringler. A multiscale nonhydrostatic atmospheric model using centroidal voronoi tessellations and C-Grid staggering. *Mon. Wea. Rev.*, 140(9):120402131411002–3105, April 2012. ISSN 1520-0493.
- 855 J. Smagorinsky. General circulation experiments with the primitive equations: I. the basic experiment*. *Mon. Wea. Rev.*, 91(3):99–164, March 1963. ISSN 1520-0493.
- Mark A. Taylor and Aimé Fournier. A compatible and conservative spectral element method on unstructured grids. *J. Comput. Phys.*, 229(17):5879–5895, August 2010. ISSN 00219991.
- J. Thuburn. Numerical wave propagation on the hexagonal c-grid. *Journal of Computational Physics*, 227(11): 860 5836–5858, May 2008. ISSN 00219991.
- J. Thuburn and C. J. Cotter. A framework for mimetic discretization of the rotating Shallow-Water equations on arbitrary polygonal grids. *SIAM Journal on Scientific Computing*, 34(3):B203–B225, January 2012. ISSN 1064-8275.
- J. Thuburn, T. D. Ringler, W. C. Skamarock, and J. B. Klemp. Numerical representation of geostrophic modes 865 on arbitrarily structured c-grids. *J. Comput. Phys.*, 228(22):8321–8335, December 2009. ISSN 00219991.
- J. Thuburn, C. J. Cotter, and T. Dubos. A mimetic, semi-implicit, forward-in-time, finite volume shallow water model: comparison of hexagonal-icosahedral and cubed-sphere grids. *Geosci. Mod. Dev.*, 7(3):909–929, May 2014.
- Hirofumi Tomita, Motohiko Tsugawa, Masaki Satoh, and Koji Goto. Shallow water model on a modified 870 icosahedral geodesic grid by using spring dynamics. *Journal of Computational Physics*, 174(2):579–613, December 2001. ISSN 00219991.
- M. Tort and T. Dubos. Dynamically consistent shallow-atmosphere equations with a complete coriolis force. *Quat. J. Roy. Met. Soc.*, 140(684):2388–2392, October 2014a. ISSN 00359009.
- M. Tort, T. Dubos, and T. Melvin. An energy-conserving quasi-hydrostatic deep-atmosphere dynamical core. 875 *Quat. J. Roy. Met. Soc.*, *accepted*, 2014a.
- Marine Tort and Thomas Dubos. Usual approximations to the equations of atmospheric motion: A variational perspective. *J. Atmos. Sci.*, 71(7):2452–2466, April 2014b.
- Marine Tort, Thomas Dubos, François Bouchut, and Vladimir Zeitlin. Consistent shallow-water equations on the rotating sphere with complete coriolis force and topography. *J. Fluid Mech.*, 748:789–821, June 2014b. 880 ISSN 1469-7645.
- Bram Van Leer. Towards the ultimate conservative difference scheme. IV. a new approach to numerical convection. *J. Comput. Phys.*, 23(3):276–299, March 1977. ISSN 0021-9991.
- H. Wan, M. A. Giorgetta, G. Zängl, M. Restelli, D. Majewski, L. Bonaventura, K. Fröhlich, D. Reinert, P. Rípodas, L. Kornbluh, and J. Förstner. The icon-1.2 hydrostatic atmospheric dynamical core on triangular grids 885 - Part 1: Formulation and performance of the baseline version. *Geosci. Mod. Dev.*, 6(3):735–763, June 2013.
- Hilary Weller, John Thuburn, and Colin J. Cotter. Computational modes and grid imprinting on five Quasi-Uniform spherical c grids. *Mon. Wea. Rev.*, 140(8):2734–2755, February 2012.

890 A. A. White and R. A. Bromley. Dynamically consistent, quasi-hydrostatic equations for global models with a complete representation of the coriolis force. *Q.J.R. Meteorol. Soc.*, 121(522):399–418, 1995. ISSN 1477-870X.

David L. Williamson. The evolution of dynamical cores for global atmospheric models. *J. Meteor. Soc. Japan*, 85B:241–269, 2007.

Appendix A: Mesh generation and smoothing

895 Among various possible ways of generating the triangular mesh, we follow the method of Sadourny et al. (1968). Starting from a spherical icosahedron made of 20 equal spherical triangles, edges are divided into equal M geodesic arcs, then the arcs joining the newly generated vertices are divided equally. The number of total grid points for resolution M is $N = 10M^2 + 2$.

900 The hexagonal mesh is constructed as the Voronoi diagram of the triangular mesh (Augenbaum and Peskin, 1985). This ensures that primal and dual edges are orthogonal, a requirement of the numerical scheme. The edge between control volumes V_i and V_j is a geodesic arc equidistant from \mathbf{G}_i and \mathbf{G}_j . A corner \mathbf{P} of a Voronoi cell is shared by three Voronoi cells and is hence equidistant from all three associated generators \mathbf{G}_i , \mathbf{G}_j and \mathbf{G}_k .

905 Numerical errors can be reduced by various optimization methods (e.g. Miura and Kimoto, 2005). We use Lloyd’s iterative algorithm (Du et al., 1999), a fixed-point iteration aimed at letting generators and centroids \mathbf{C}_i of control volumes coincide :

$$\mathbf{C}_i = \frac{\int_{V_i} \mathbf{x} \, dA}{\left\| \int_{V_i} \mathbf{x} \, dA \right\|}. \quad (\text{A1})$$

910 The optimization process is efficient for coarse grids but tends to stagnate at high grid resolution (Du et al., 2006). Therefore we simply stop the optimization process after a fixed user-defined number iterations. Optimization is performed only once during the grid generation and even a few thousand iterations are computationally not very costly.

Appendix B: Accurate and stable spherical primitives

915 Although round-off errors may not be an urgent concern with double-precision computations at presently common resolutions, it may become if formulae with high round-off error are used in sequence, if single precision is used for speed, or at high resolutions. In this Appendix we describe geometric primitives that are not sensitive to round-off error, or more precisely that are not more sensitive to round-off errors than equivalent planar primitives. This primitives are required in the grid generation and optimization process and compute centroids, circumcenters and spherical areas.

Let \mathbf{G}_i , \mathbf{G}_j and \mathbf{G}_k be generators in anti-clockwise order. The sides of spherical triangle $\mathbf{G}_i\mathbf{G}_j\mathbf{G}_k$ are $O(h)$ with $h \sim 1/M$ small and the vectors \mathbf{G}_i , \mathbf{G}_j and \mathbf{G}_k are known up to a round-off er-

920 for ϵ . The circumcenter \mathbf{p} is a unit vector equidistant from each generator. Using the fact that $\mathbf{G}_i, \mathbf{G}_j, \mathbf{G}_k, \mathbf{p}$ have unit norm and some algebra yields the system :

$$\mathbf{p} \cdot \mathbf{p} = 1, \quad (\mathbf{G}_j - \mathbf{G}_i) \cdot \mathbf{p} = (\mathbf{G}_k - \mathbf{G}_i) \cdot \mathbf{p} = (\mathbf{G}_j - \mathbf{G}_k) \cdot \mathbf{p} = 0. \quad (\text{B1})$$

A solution of (B1) is given by

$$\mathbf{p} = \frac{\mathbf{p}_1}{\|\mathbf{p}_1\|} \quad \text{where } \mathbf{p}_1 = (\mathbf{G}_i - \mathbf{G}_j) \times (\mathbf{G}_i - \mathbf{G}_k), \quad (\text{B2})$$

925 used for instance by Miura and Kimoto (2005). Due to finite precision the computation of $(\mathbf{G}_i - \mathbf{G}_j) \times (\mathbf{G}_i - \mathbf{G}_k)$ has an error $O(\epsilon h)$. Furthermore \mathbf{p}_1 is $O(h^2)$. Therefore (B2) yields \mathbf{p} with an error which is $O(\epsilon/h)$. In order to avoid dividing a by the small factor $\|\mathbf{p}_1\|$, we take advantage of the fact \mathbf{p} is close to \mathbf{G}_i . Hence it is better to solve for $\mathbf{p} - \mathbf{G}_i$, which yields

$$\mathbf{p} = \frac{\mathbf{p}_2}{\|\mathbf{p}_2\|} \quad \text{where } \mathbf{p}_2 - \mathbf{G}_i = \frac{\mathbf{p}_1}{2\mathbf{p}_1 \cdot \mathbf{p}_1} \times (\|\mathbf{G}_j - \mathbf{G}_i\|^2(\mathbf{G}_i - \mathbf{G}_k) + \|\mathbf{G}_k - \mathbf{G}_i\|^2(\mathbf{G}_j - \mathbf{G}_i)). \quad (\text{B3})$$

930 Each input to $\mathbf{p}_2 - \mathbf{G}_i$ has a relative error $O(\epsilon/h)$ and $\mathbf{p}_2 - \mathbf{G}_i$ itself is $O(h)$, yielding an overall absolute error $O(\epsilon)$. Now \mathbf{p}_2 is $O(1)$ and known within $O(\epsilon)$, hence \mathbf{p} as well. In order to check the accuracy of formulae (B2,B3) we present in figure (6) $Err = \max_{l,m=i,j,k} \|(\mathbf{p} - \mathbf{G}_l)^2 - (\mathbf{p} - \mathbf{G}_m)^2\|$ for a random set of spherical triangular cells of decreasing size. With the direct formula (B2) Err increases as the triangle size decreases (as predicted by the scaling $Err \sim \epsilon/h$), demonstrating the sensitivity of (B2) to round-off error. (B2) becomes useless when $h \sim \epsilon/h$ which would happen with single-precision calculations at resolutions of about 1/1000 the planetary radius, i.e. 6km on Earth. Conversely (B3) is stable and determines the position of \mathbf{p} within round-off error.

Regarding the spherical center of mass (A1), an exact Gauss formula exists for polygonal control
 940 volumes (not shown). Again this formula has large cancellation errors and yields \mathbf{C}_i with a round-off error $O(\epsilon/h)$. For a spherical triangle, the planar center of mass (equal-weight barycenter) projected onto the unit sphere yields a third-order accurate estimate of the true center of mass. Therefore subdividing a polygon into spherical triangles and forming an area-weighted sum of their barycenters yields a second-order accurate estimate of \mathbf{C}_i . This accuracy is sufficient for our purposes. An
 945 accurate and stable alternative is to decompose polygons into triangles and quadrangles, map the unit square to a spherical quadrangle or triangle and use high-order Gauss-Legendre quadrature to evaluate (A1).

Finally computing the area A of a spherical polygon should not be done using the simple but again unstable defect formula. Instead we decompose polygons into triangles and use l'Huilier formula :

$$950 \quad \tan \frac{A}{4} = \sqrt{\tan \frac{s}{2} \tan \frac{s-a}{2} \tan \frac{s-b}{2} \tan \frac{s-c}{2}} \quad (\text{B4})$$

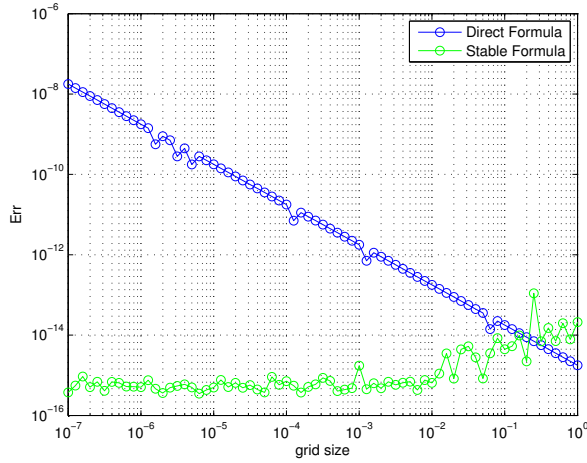


Figure 6: Error in circumcenter calculation using direct formula (B2) and stable formula (B3). For a given value of the grid size h , the triangle is defined by three points on the unit sphere $\mathbf{a}, \mathbf{b}/\|\mathbf{b}\|, \mathbf{c}/\|\mathbf{c}\|$ where $\mathbf{b} = \mathbf{a} + h\tilde{\mathbf{b}}, \mathbf{c} = \mathbf{a} + h\tilde{\mathbf{c}}$ and $\tilde{\mathbf{b}}, \tilde{\mathbf{c}}$ are random vectors whose Cartesian components are statistically independent, centered, Gaussian random variables with unit variance. For each h , 100 $\tilde{\mathbf{b}}, \tilde{\mathbf{c}}$ are generated and the largest error is reported.

where A is the desired triangular area, $2s = a + b + c$ and a, b, c are the geodesic lengths of the sides of the triangle, computed as $\text{dist}(\mathbf{p}, \mathbf{q}) = \sin^{-1} \|\mathbf{p} \times \mathbf{q}\|$. Formula (B4) reduces for small triangles to the planar Heron formula, which demonstrates its stability.